

# Lunar Pole Illumination and Communications Maps Computed from Goldstone Solar System Radar Elevation Data

Scott Bryant\*

The Goldstone Solar System Radar (GSSR) group at JPL produced a digital elevation model (DEM) of the lunar south pole using data obtained in 2006. This new DEM has 40-m horizontal resolution and about 5-m relative vertical accuracy. This article explains how this DEM was used to evaluate average solar illumination and Earth visibility near the lunar south pole. The elevation data were converted into local terrain horizon masks for the area within 100 km of the lunar south pole. These topocentric horizon masks were converted into selenographic latitude and longitude coordinates, then compared to regions bounding the maximum Sun and Earth motions relative to the Moon. Estimates of Earth visibility were computed by integrating the area of the region bounding the Earth's motion that was below the horizon mask. Solar illumination and other metrics were computed similarly. Proposed lunar south pole base sites are examined in detail, with the best site showing multiyear averages of solar power availability of 92 percent and direct-to-Earth (DTE) communication availability of 51 percent. Results are compared with a theoretical model and with actual Sun and Earth visibility averaged over the years 2009 to 2028. Peaks near the lunar south pole with continuous DTE communications are also presented. Results for the lunar north pole were computed using the GSSR DEM of the lunar north pole produced in 1997. The article also explores using a heliostat to reduce the photovoltaic power system mass and complexity.

## I. Introduction

Because of the 1.54-deg inclination of the Moon's rotation pole to the ecliptic plane, the Sun never rises more than a few degrees of elevation angle above the horizon at the lunar polar regions. Many depressions and crater floors near the poles are permanently shaded from the Sun, producing a permanent low-temperature area. These permanently shaded areas may be reservoirs for water ice deposits [1]. The potential for using lunar ice to produce oxygen, hydrogen fuel, and drinking water is driving investigations of human exploration bases at the lunar poles [2].

---

\* Communications Ground Systems Section; Space Communications and Navigation (SCaN) Lunar Architecture Study Group.

The research described in this publication was carried out by the Jet Propulsion Laboratory, California Institute of Technology, under a contract with the National Aeronautics and Space Administration. © 2009 California Institute of Technology. Government sponsorship acknowledged.

The same geometry that creates permanently shadowed regions in lunar polar craters also increases solar illumination on lunar polar mountains. A typical lunar surface location is exposed to the Sun for half of the 29.5-day synodic month, but a tall peak near the lunar poles could view the Sun during the entire synodic month. These “peaks of eternal light” [3] would provide base sites with near-continuous solar power and illumination [4,5]. The analysis presented here shows no peak of eternal light at either lunar pole, but shows several locations with more than 90 percent solar illumination averaged over several lunar years.

Evaluating the resource potential of lunar polar base sites is a high priority for future lunar exploration [6]. This includes determining the amount of direct-to-earth (DTE) communications available from the polar base locations. The orbital mechanics causing the lunar librations seen from Earth also cause the Earth to move across several degrees of elevation and azimuth in the lunar sky. Even though the Moon is tidally locked, the Earth appears to move +6.87 deg in latitude and +8.16 deg in longitude.<sup>1</sup> Therefore, lunar polar base DTE communications are only possible about half of each sidereal month (27.3 days). This article presents multiyear averages of solar illumination, solar power, and Earth visibility metrics for the lunar pole regions to help evaluate base sites.

## II. Background

The latest Goldstone Solar System Radar (GSSR) DEM was produced by the GSSR group at JPL from observations taken during September 2006. The GSSR group uses antennas in NASA’s Deep Space Network to produce radar images of solar system objects [7] using interferometry techniques. These data were acquired during lunar librations that increased the view of the lunar south pole. The Earth’s selenographic latitude during the data acquisition was 6.2 deg south, allowing the GSSR to see lunar terrain several degrees toward the farside of the lunar south pole. The GSSR group processed the radar data into a DEM in lunar polar stereographic projection coordinates. The DEM covers an area approximately 880 km from nearside to farside and 500 km east to west across the lunar south pole. The DEM covers the lunar south pole out to 70 km toward the lunar farside and farther in the other directions.

The DEM uses a polar stereographic Cartesian coordinate system centered on the lunar south pole, with X-axis pointed east (90 deg lunar east longitude), and Y-axis pointed nearside (0 deg lunar east longitude). Figure 1 shows the lunar south pole region of the 2006 DEM data, along with some lunar features. The lunar south pole is on the rim of Shackleton Crater. Figure 2 shows the lunar north pole region of the 1997 DEM data, with some lunar features. The gray areas in both figures were not visible from Earth during the radar imaging. Both figures show two-letter designations of proposed base sites used in this article. The base site lettering is derived from the base site identification used in [4]. Most feature names and locations are from the International Astronomical Union (IAU) lunar naming in the *Gazetteer of Planetary Nomenclature*;<sup>2</sup> however, some of the mountain peaks use older, unofficial names [8].

---

<sup>1</sup> R. Roncoli, “Lunar Constants and Models Document,” JPL D-32296 (internal document), Jet Propulsion Laboratory, Pasadena, California, September 23, 2005.

<sup>2</sup> International Astronomical Union, IAU Gazetteer of Planetary Nomenclature. <http://planetarynames.wr.usgs.gov>

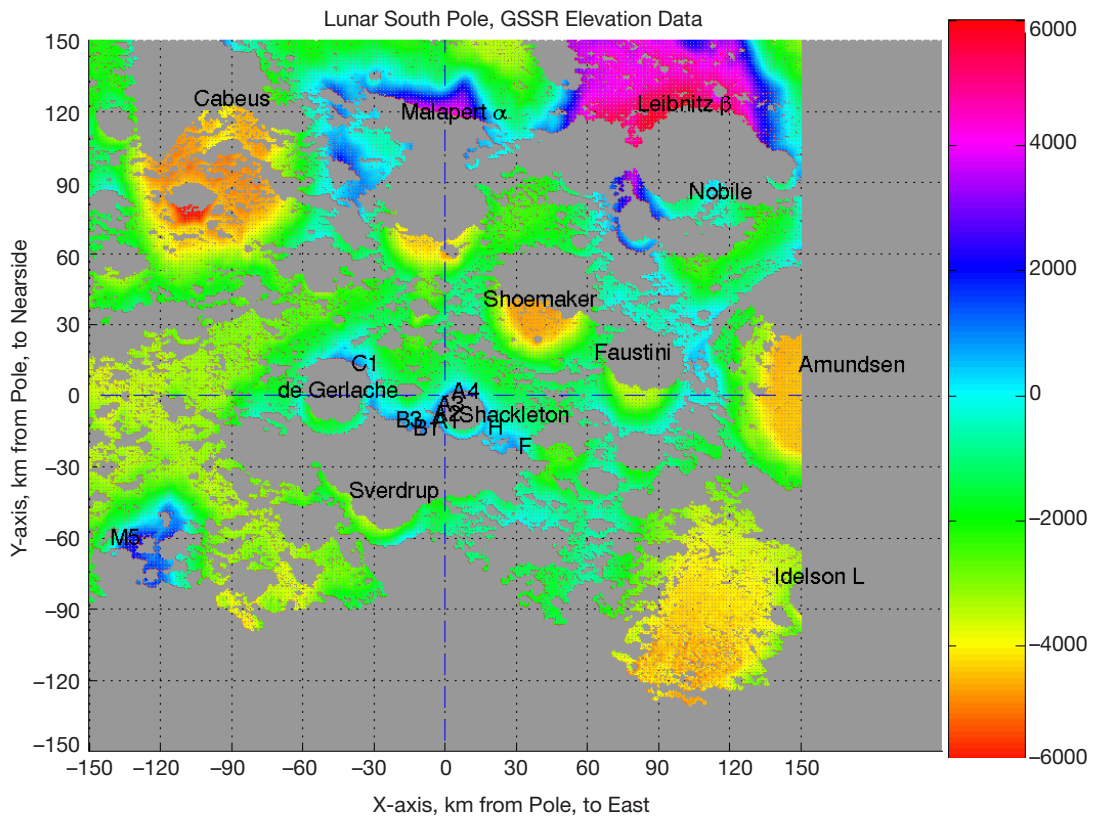


**Figure 1.** Lunar south pole elevation map from GSSR 2006 DEM.

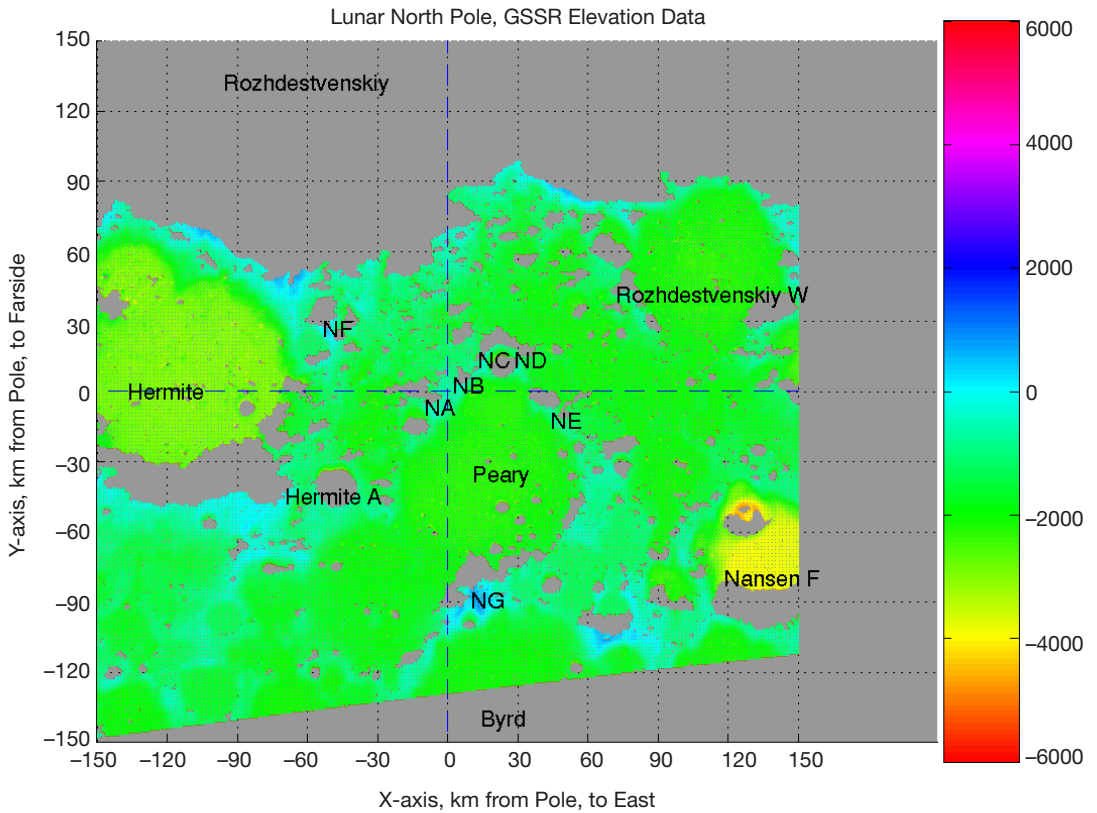


**Figure 2.** Lunar north pole elevation map from GSSR 1997 DEM.

Figure 3 shows the proposed lunar south pole base locations around Shackleton Crater. The figure reveals the high resolution of the 2006 south pole radar DEM. The 40-m spatial resolution of the data produces a topographic map with good internal consistency and rich detail. Inside Shackleton Crater, the missing elevation data within the radar shadow were filled in with values based on a parabolic elevation profile. Figure 3 also indicates that the rim of Shackleton Crater covers a horizontal distance of about 200 m (5 data points), instead of being an abrupt scarp. This suggests the actual DEM point-to-point elevation error is close to the stated relative vertical accuracy of 5 m [7]. Based on this vertical accuracy, the analysis used 2-m-tall towers for the baseline horizon mask computations.

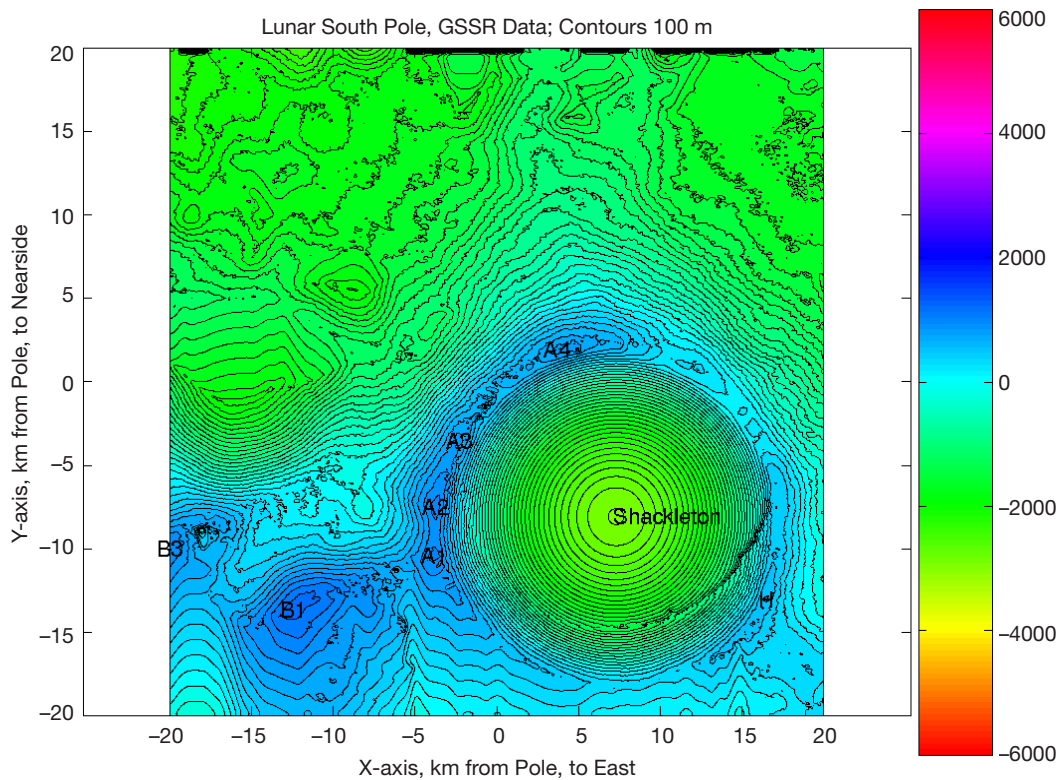


**Figure 3. Shackleton Crater topographic map, with base sites.**

Table 1 lists lunar pole features and their locations in both lunar coordinate systems.<sup>3</sup> Some feature names are not official IAU names [8]. Crater locations are for the apparent center of the crater. Proposed base site locations are given later in this article.

### III. Analysis Method

Analyzing the DEM to produce solar illumination and DTE communications required several major steps. Step 1 corrected the DEM elevations by removing bad points and filling in radar shadow areas with approximate elevations. Step 2 computed horizon masks from the

---

<sup>3</sup> International Astronomical Union, IAU Gazetteer of Planetary Nomenclature. <http://planetarynames.wr.usgs.gov>

**Table 1. Lunar north and south pole feature coordinates.**

Feature	Pole	X, km	Y, km	Latitude	Longitude	Crater Diameter or Mountain Elevation, km
Malapert $\alpha$	S	3.56	119.60	-86.037	1.705	4.207
Leibnitz $\beta$	S	101.32	123.04	-84.723	39.471	6.055
M5	S	-134.95	-59.97	-85.110	-113.960	2.557
Amundsen Crater	S	171.67	13.21	-84.300	85.600	156.000
Cabeus Crater	S	-89.45	125.40	-84.900	-35.500	98.000
de Gerlache Crater	S	-45.22	2.29	-88.500	-87.100	32.400
Faustini Crater	S	79.42	18.34	-87.300	77.000	39.000
Idel'son L Crater	S	157.74	-76.26	-84.200	115.800	28.000
Malapert Crater	S	34.39	150.14	-84.900	12.900	69.000
Nobile Crater	S	116.53	86.22	-85.200	53.500	73.000
Shackleton Crater*	S	7.32	-8.08	-89.639	137.825	19.000
Shackleton Crater**	S	0.00	3.02	-89.900	0.000	19.000
Shoemaker Crater	S	40.48	40.62	-88.100	44.900	50.900
Sverdrup Crater	S	-21.26	-39.98	-88.500	-152.000	35.000
Byrd	N	24.16	-139.86	85.300	9.800	93.000
Hermite	N	-120.78	-0.21	86.000	-89.900	104.000
Hermite A	N	-48.65	-45.21	87.800	-47.100	20.000
Nansen F	N	138.63	-80.04	84.700	60.000	62.000
Peary	N	23.01	-35.44	88.600	33.000	73.000
Rozhdestvenskiy	N	-60.34	131.80	85.200	-155.400	77.000
Rozhdestvenskiy W	N	113.49	41.31	86.000	110.000	75.000

\* From GSSR values. \*\* IAU values.

DEM information. Topocentric horizon masks were computed for a viewpoint at 2 m altitude above the surface and then converted into selenographic (lunar-centered) equatorial latitude and longitude coordinates. Step 3 estimated multiyear average illumination metrics by comparing the horizon mask in selenographic latitude and longitude to a uniform distribution of the Sun and Earth exposure in selenographic coordinates. This step assumed a simplified time average for the solar and Earth motions as seen from the Moon, eliminating the astrodynamics calculations. Step 4 collected these multiyear average illumination and DTE visibility metrics for areas around the lunar south pole. Those metrics are presented as contour plots, tables, and horizon masks.

The analysis was then extended using actual Sun and Earth positions as seen from the lunar poles. The multiyear average illumination and DTE metrics were computed using actual Sun and Earth positions for the years 2009 to 2028. In addition, a theory was developed for multiyear average illumination and DTE visibility as a function of lunar location and altitude above the lunar surface. The metrics from Step 3 and the metrics using actual positions were then recomputed for several heights above the lunar surface, and compared with the developed theory.

#### **A. Step 1: Correcting DEM Elevation and Filling Radar Shadows**

During the 2006 GSSR data acquisition, Earth was at about 6.2 deg south selenographic latitude. This placed Earth at approximately +6.2 deg of elevation angle as seen from the lunar south pole. Therefore, some parts of the polar terrain were not visible to the radar. For the 100 km × 100 km area centered on the lunar south pole, about 40 percent of the area was not imaged because it was in radar shadow. In addition, several imaged areas had very low radar backscatter signal strength, leading to spurious elevation values. Several locations next to the radar shadow edge have erroneous elevation values. These features of the GSSR DEM required correction prior to using the DEM for illumination computations.

MATLAB was used for most of the computation, including the data corrections. First, the 2006 GSSR DEM file of elevations and the file of backscatter magnitudes were read into MATLAB. Because of the large file size, the program read a data subset covering the 100 km × 100 km area at full 40-m resolution (2501 × 2501 pixels) centered on the lunar south pole. For coarser far-field computations, the program read in a 400 km × 400 km area and decimated it to 600-m resolution by taking every 15th point (667 × 667 pixels). The program then edited the DEM elevations to remove known artifacts. Specifically, the areas ( $-8.5 \text{ km} < X < -7 \text{ km}$ ,  $-14.5 \text{ km} < Y < -13.5 \text{ km}$ ) and ( $-7 \text{ km} < X < -3 \text{ km}$ ,  $-16 \text{ km} < Y < -12 \text{ km}$ ) were scanned and all elevations greater than 800 m were set to the value of the radar shadow areas (-10,000 m). This removed two steep-sided “towers” on a ridgeline west of Shackleton Crater. GSSR experts at JPL confirmed these two “towers” were probably anomalies from the elevation processing algorithms. The remaining area covered by elevation data was 6180 km<sup>2</sup>, or 61.8 percent of the 100 km × 100 km original area.

The MATLAB program then pruned out elevations with local slopes in excess of 60 deg. For the 100 km × 100 km area centered on the lunar south pole, this removed 1.7 percent of the remaining elevation data. Next, the program removed elevation points with radar backscatter value less than 0.06 percent. For the 100 km × 100 km area, this removed 18.3 percent of the remaining elevation data. Several elevation anomalies were eliminated by these slope and backscatter limits, including hilly terrain inside the nearside–east rim of Shackleton Crater. This hilly terrain was determined to be a processing artifact, because it would have obscured Earth’s view of other radar-imaged terrain inside Shackleton Crater.

The MATLAB program then scanned the remaining elevation values and removed any points with less than four surrounding points. This removed almost all small “islands” of isolated elevation data, which had proven to be mostly artifacts of the radar processing. This step removed 0.5 percent of the elevation data. The cumulative effect of the data editing removed about 21 percent of the original elevation data in the 100 km × 100 km map. This reduced the elevation data coverage from 6180 km<sup>2</sup> to 4916 km<sup>2</sup> or from 61.8 percent to 49.2 percent of the 100 km × 100 km map. Similar percentages were removed for the larger coarse maps.

The MATLAB program then created elevation data to fill in the missing points. Inside Shackleton Crater, the program created a parabolic surface with a center elevation of -2900 m at  $X = 7.32 \text{ km}$ ,  $Y = -8.08 \text{ km}$ . This produced a more realistic three-dimensional

plot of the crater, but did not affect the illumination results. For the remaining radar shadow and edited areas, the program set the elevation values to the altitude of the radar shadow. The program scanned each column of elevation data from the +Y to -Y direction. At each missing data location, the program computed a straight line from Earth at 6.2 deg south selenographic latitude that passed through the last known +Y elevation data value. This means the elevation in the unknown terrain was set to values just under the GSSR radar shadow envelope. This models an upper bound on the possible elevations. If the actual elevations were higher, then the point would have appeared on the radar. This upper bound provides a conservative estimate for solar illumination computations. Actual terrain elevations inside the radar shadow area are probably lower than the radar line of sight, and would block less of the surrounding terrain. The program also set a lower limit of -5000 m elevation to prevent elevation estimates toward the lunar farside from becoming excessively deep.

Similar pruning was applied to the lunar north pole DEM from 1997. The MATLAB program read in a 400 km × 400 km area at the 600-m resolution of the DEM. The same data pruning algorithms were applied, but no specific elevation artifacts were targeted for removal.

#### B. Step 2: Horizon Mask Computation

The horizon masks were computed by scanning along lines of constant azimuth. For convenience in computation, the line of 0 azimuth was always parallel to the lunar prime meridian at 0 deg longitude, not due north. This made the conversion to the final equatorial coordinates easier and did not affect the results. Maps were selected with “coarse” or “fine” grid resolution, as described below. For each point on the grid, the MATLAB program defined a circle around the point, then scanned along lines of azimuth for at least 200 km. This 200-km distance was determined from a requirement to examine far enough along the azimuth lines to find any peaks that would block the Sun. At mid-winter, the Sun will be at an elevation angle of -1.54 deg as seen from the lunar south pole. The tallest peak near the lunar south pole is Leibnitz  $\beta$ , at an elevation of 6055 m. As shown in Figure 4, the lunar horizon falls off quickly with distance. The plot indicates that at 200 km from the pole, a mountain must be over 7000 m tall in order to block the winter Sun. This gave a practical limit of 200 km for the distance to use in examining the lines of azimuth. This also set the size necessary for the DEM subsets around the lunar pole.

The elevation angles were computed starting at the grid point at the center of the horizon mask and extending out to points on the lunar terrain along each azimuth line. The maximum elevation angle for each azimuth was stored in an array of horizon mask elevation versus azimuth. The horizon mask results depend on the altitude of the observer at the horizon mask center. Unless otherwise stated, an observation tower 2 m above the local terrain was used for the horizon mask computations. This represented a practical height for solar array installation. For some locations, additional horizon mask metrics were computed using taller towers.

Coarse-resolution horizon masks were computed from a DEM decimated to 600-m spatial resolution that covered a 400-km grid centered on the lunar south pole. The lines of azimuth were spaced 5 deg apart. Maps were generated covering 30 km × 30 km areas

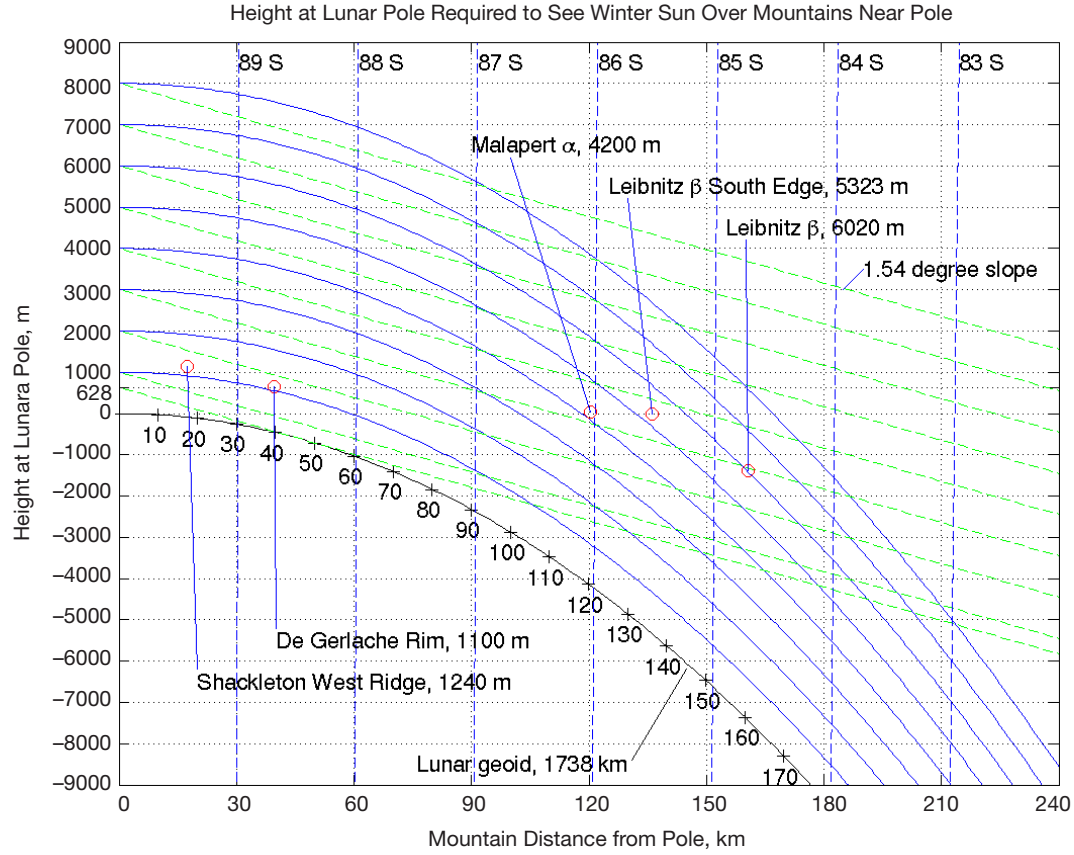


**Figure 4. Solar lines of sight at the lunar south pole.**

( $51 \times 51$  pixels). A total of 64 maps were generated to cover the region within 110 km of the lunar south pole. For the lunar north pole, maps were generated in the same way. Because there are no extremely tall mountains to consider near the lunar north pole, fewer maps were examined. A total of 42 maps were generated, covering the regions within 105 km of the lunar north pole, except the farside, which was covered to 75 km.

For the lunar south pole, medium-resolution horizon masks were computed for specific areas of interest identified from the coarse-resolution maps. The medium-resolution masks used two DEMs: a coarse DEM decimated to 1000-m spatial resolution that covered a 400-km grid centered on the lunar south pole, and a fine DEM at 40-m spatial resolution that covered a 12-km grid centered on the location of interest. This 12 km  $\times$  12 km area was removed from the coarse DEM prior to the elevation angle computations. Horizon masks were computed for both DEMs using azimuth spacing of 5 deg. Then, for each azimuth, the greater elevation angle of the two horizon masks was selected for the composite horizon mask. This two-DEM approach produced a higher-resolution result while keeping the computation time reasonably short. Maps were generated covering 1 km  $\times$  1 km areas with resolution of 40 m ( $51 \times 51$  pixels).

For a small number of locations, fine-resolution horizon masks were computed using two DEMs: a coarse DEM decimated to 1000-m spatial resolution that covered a 400-km grid centered on the lunar south pole, and a fine DEM at 40-m spatial resolution that covered

a 100-km grid centered on the lunar south pole. This  $100\text{ km} \times 100\text{ km}$  area was removed from the coarse DEM prior to the elevation angle computations. Horizon masks were computed for both DEMs using azimuth spacing of 1 deg. Then, for each azimuth, the greater elevation angle of the two horizon masks was selected for the composite horizon mask. This two-DEM approach produced a higher-resolution result, while keeping the computation time reasonably short. Horizon masks were computed for single-point locations, and extra solar illumination and Earth visibility metrics were created from the horizon masks. The fine-resolution computations were performed only at locations with high solar illumination found from the coarse- and medium-resolution maps.

### C. Step 3: Computing Illumination Metrics from Average Solar and Earth Motion

Figure 5 shows a horizon mask profile in lunar topographic azimuth and elevation coordinates. This mask was produced with 1-deg azimuth steps using the “fine” resolution technique described above. The figure shows areas defining the limits for Earth and solar motion as seen from the Moon. In selenographic coordinates, the Earth’s center is confined to a maximum east–west longitude libration of 8.16 deg, and a north–south latitude libration of 6.87 deg.<sup>4</sup> These libration values are the maximum possible librations, not the typical average values. In topocentric coordinates, the maximum excursion of Earth’s center is shown by the parallelogram marked with red circles. Earth’s disk subtends an angle of 1.9 deg as seen from the Moon. Therefore, the limbs of the Earth will extend beyond the box defined above. The limits of the motion of Earth’s South Pole are shown by the parallelogram marked with red upward-pointing triangles. The limits of the motion of Earth’s North Pole are shown by the parallelogram marked with red downward-pointing triangles.

The Sun moves across all degrees of longitude, but is confined to latitudes between 1.54 deg north and south. The motion of the Sun’s center is plotted with yellow circles. The solar disk subtends an angle of 0.53 deg as seen from the Moon. The motion of the northern and southern limbs of the Sun are shown with yellow lines. The boundary limit of the solar path is lowest on the horizon in the direction of the lunar south pole, at azimuth =  $\arctan(x/y)$  or 42.2 deg. Note the sinusoidal shape of the solar limits in the azimuth–elevation coordinate frame of Figure 5. This sinusoidal shape is due to the coordinate transformation from selenographic latitude–longitude to a local topocentric frame centered away from the lunar pole. In this local topocentric frame, lines of constant selenographic latitude are not lines of constant elevation.

Figure 6 shows the same information as Figure 5, but expressed in selenographic coordinates. The selenographic coordinate frame has 0 deg of latitude in directions parallel to the lunar equator, and 0 deg of longitude in directions parallel to the nearside prime meridian facing Earth. In the selenographic coordinate frame, the Earth and Sun maximum limits are defined by rectangles of constant latitude and longitude. Note that Figure 6 defines south latitude as positive, so that the lunar terrain horizon mask for this lunar south pole location appears “right side up” when compared to Figure 5. Figure 6 shows that the lunar terrain

---

<sup>4</sup> R. Roncoli, op. cit.

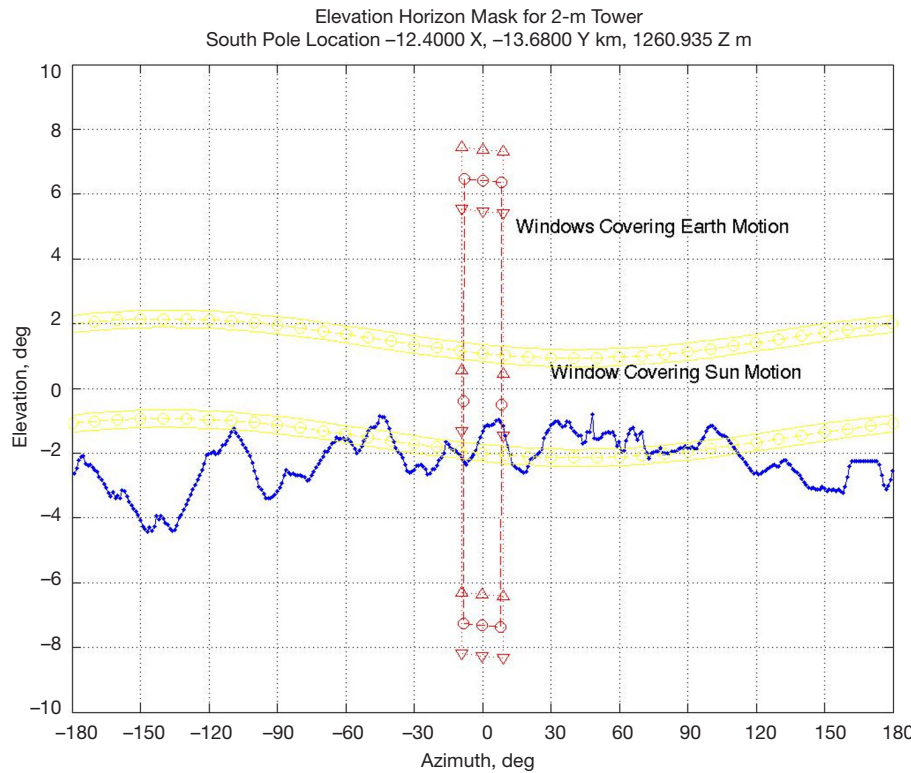


**Figure 5.** Site B1 terrain horizon mask with 1-deg azimuth spacing.

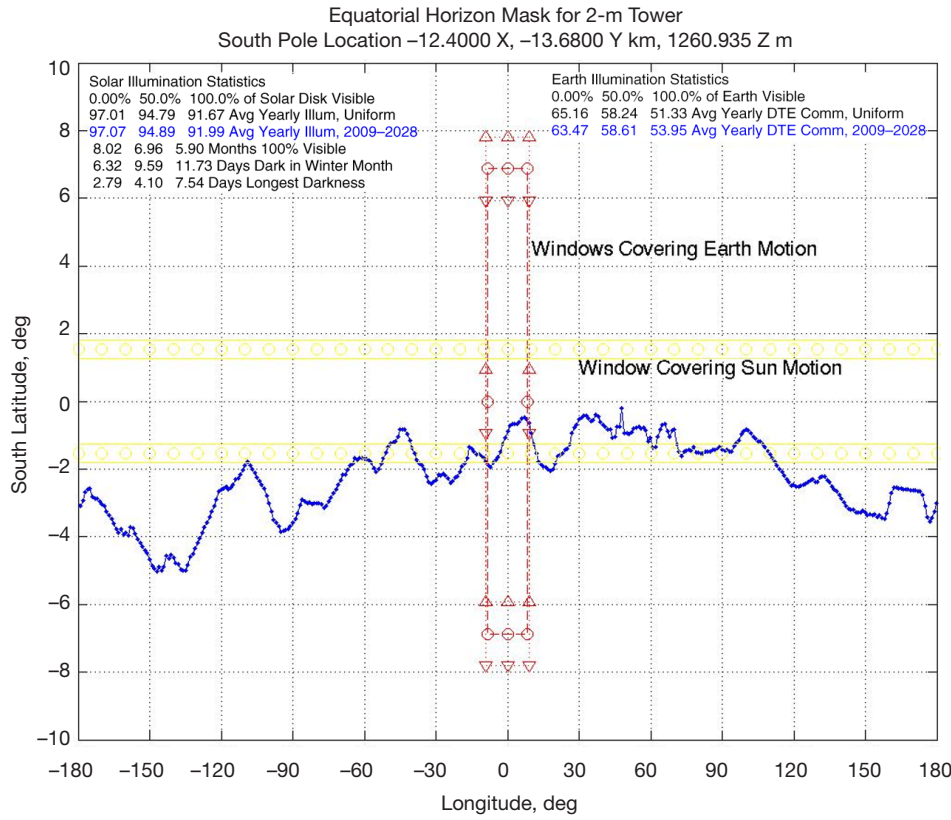


**Figure 6.** Site B1 terrain horizon mask with 1-deg azimuth spacing, in selenographic coordinates.

horizon mask has shifted with the transformation to selenographic coordinates, raising up in the direction of the lunar south pole at 42.2 deg longitude, and dipping down in the direction of the lunar north pole at -137.8 deg longitude.

The following assumptions were made to simplify computing multiyear averages of the solar illumination and Earth visibility:

- (1) In selenographic coordinates, the centers of the Sun and Earth stay inside the bounding rectangles defining the maximum longitude and latitude excursions. The center of the solar disk stays within a rectangle defined by east-west longitudes 180 deg, and north-south latitudes of 1.54 deg. The center of Earth's disk stays within east-west longitudes 8.16 deg and north-south latitudes 6.87 deg.
- (2) Averaged over many years, the Sun and Earth motions bring them to all locations within their bounding rectangles. Particularly, during the 18.6-yr period of the regression of the longitude of the ascending node, the Earth will cover all locations within its bounding rectangle.
- (3) Averaged over many years, the Sun has an equal probability of being at any location within its bounding rectangle. A similar assumption is made for Earth within its bounding rectangle. This assumption is less accurate for Earth, since Earth does not reach the extremes of latitude libration in every year.

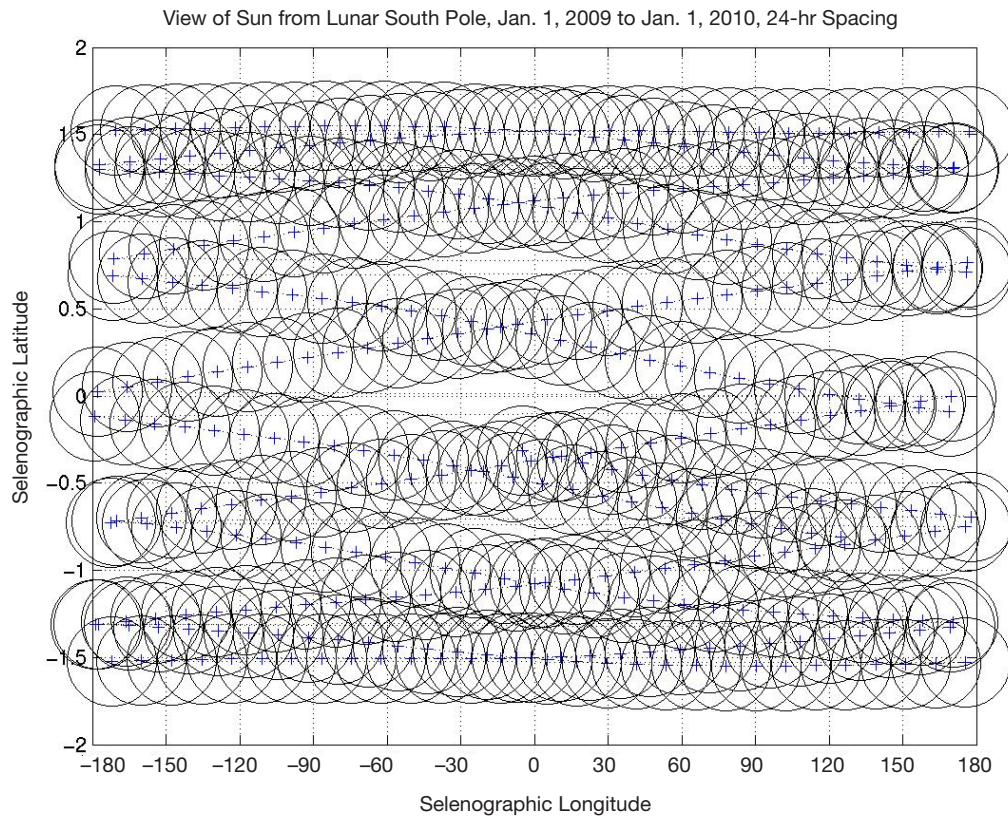
These assumptions bypass computing the exact location of the Sun and Earth at specific times of interest. Instead, the illumination computations use the area of the bounding rectangles in Figure 6. The validity of assumptions 1 and 2 are shown in Figures 7 through 10. The data for these figures were computed using the Jet Propulsion Laboratory (JPL) HORIZONS on-line solar system data and ephemeris computations service.<sup>5</sup> Figures 7 through 10 use data computed for an observer at the lunar south pole with data points every 24 hr. Figures 7 through 10 define north latitude as positive.

Figure 7 shows the view of the Sun in selenographic latitude and longitude for the period January 1, 2009, to January 1, 2010. The black circles show the disk of the sun centered on the blue cross of each data point. Figure 8 shows the view of the Sun in selenographic latitude and longitude for the period January 1, 2009, to January 1, 2028. The blue crosses show the center of the Sun for each data point. These figures indicate that assumptions 1 and 2 agree with the actual ephemeris data. Figure 8 indicates that the solar distribution across the bounding rectangle is uniform in longitude, but not latitude. The Sun appears to spend more time at the north and south latitude limits than in the center. However, between 1.2 deg north and south latitude, the solar distribution appears roughly uniform.

Figure 9 shows the view of Earth in selenographic latitude and longitude for the period January 1, 2009, to January 1, 2010. The black circles show the disk of Earth centered on the blue cross of each data point. The red rectangle shows that the assumed bounding rectangle of the center of Earth's disk within east-west longitudes 8.16 deg and north-south latitudes

---

<sup>5</sup> <http://ssd.jpl.nasa.gov/?horizons>



**Figure 7.** Lunar south pole ephemeris data for the Sun, 2009 to 2010.

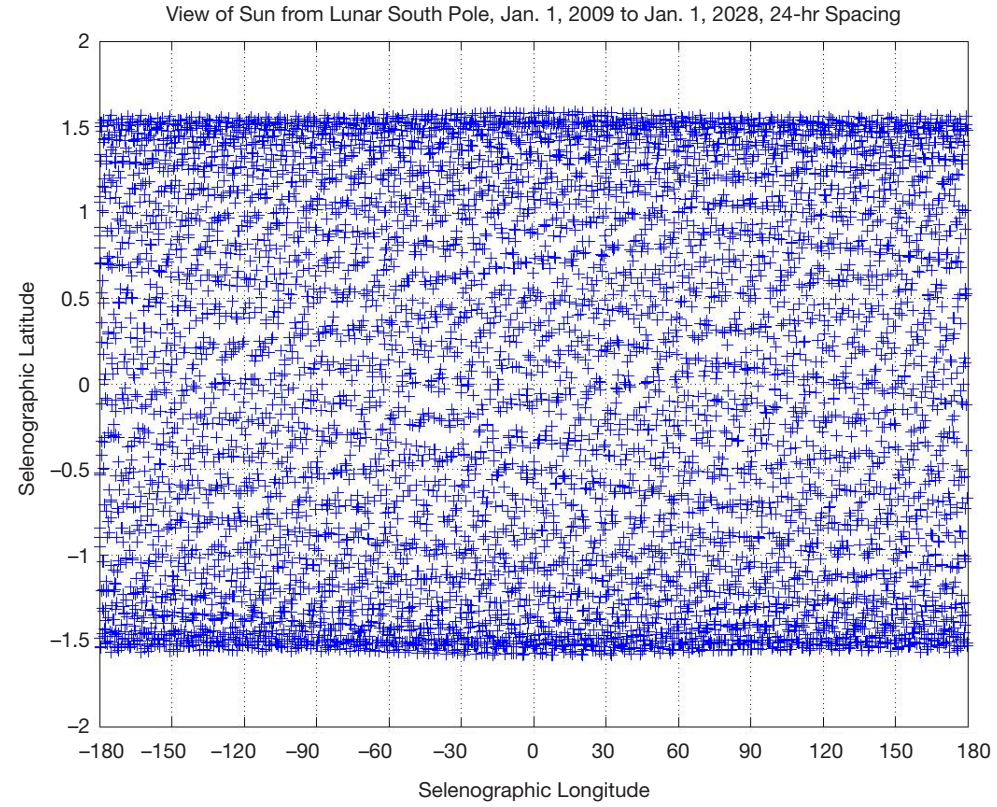


**Figure 8.** Lunar south pole ephemeris data for the Sun, 2009 to 2028.

6.87 deg. Over the year 2009, Earth does not cover the entire bounding rectangle, but traces an approximation to a Lissajous curve between the lower left and upper right corners.

Figure 10 shows the view of Earth in selenographic latitude and longitude for the period January 1, 2009, to January 1, 2028. The blue crosses show the center of Earth for each data point. These figures indicate that assumptions 1 and 2 agree with the actual ephemeris data. Figure 10 indicates that the Earth distribution across the bounding rectangle is somewhat uniform in longitude, but not latitude. Earth appears to spend more time at the north and south latitude limits than in the center. However, over this 19-yr interval, Earth's disk will cover every point in the bounding rectangle. The assumption of a uniform distribution across the bounding rectangle will be examined in more detail later in this article.

The illumination metrics in the next step are based on how much area of the bounding rectangle is covered by the terrain horizon mask. The assumptions 1 through 3 mean that the illumination metrics will not be exact for a particular date, but will be representative of a multiyear average value. These averaged values allow comparisons between different lunar sites, since the only variable is the lunar terrain at the different locations. These assumptions greatly reduced the amount of computation needed for computing illumination and Earth visibility metrics.

#### **D. Step 4: Collecting Solar Illumination and DTE Visibility Metrics**

Based on the assumptions above, several metrics were computed from horizon masks projected into the lunar selenographic coordinates. Average solar illumination was computed by integrating the area of the Sun's bounding rectangle above the horizon mask. The integrated area was then normalized with the area of the entire solar bounding rectangle, resulting in the percentage of time that the Sun is visible. Three types of solar illumination averages were computed, varying with the amount of visible solar disk (see Figure 6). Since the solar disk radius is 0.265 deg as seen from Earth's orbit, the metrics vary with the amount of the solar disk covered.

The "0 percent of solar disk visible" is the average computed by integrating the horizon mask over the solar bounding rectangle from 1.275 deg north to 1.805 degrees south latitude. Using the convention shown in Figure 6, defining south latitude as positive, this integration covers from -1.275 deg to +1.805 deg latitude. This metric requires that the horizon mask cover the entire solar disk, up to the southern limb, to not count as illuminating the lunar terrain. This metric represents the amount of time that any solar light is available.

The "50 percent of solar disk visible" metric integrated the horizon mask over the solar bounding rectangle from -1.54 deg to +1.54 deg latitude. This metric requires that the horizon mask cover more than half the solar disk to not count as illuminating the lunar terrain. This metric represents half-strength solar illumination.

The "100 percent of solar disk visible" metric integrated the horizon mask over the solar bounding rectangle from -1.805 deg to +1.275 deg latitude. This metric requires that the horizon mask merely touch the solar disk at the northern limb, to not count as illuminat-

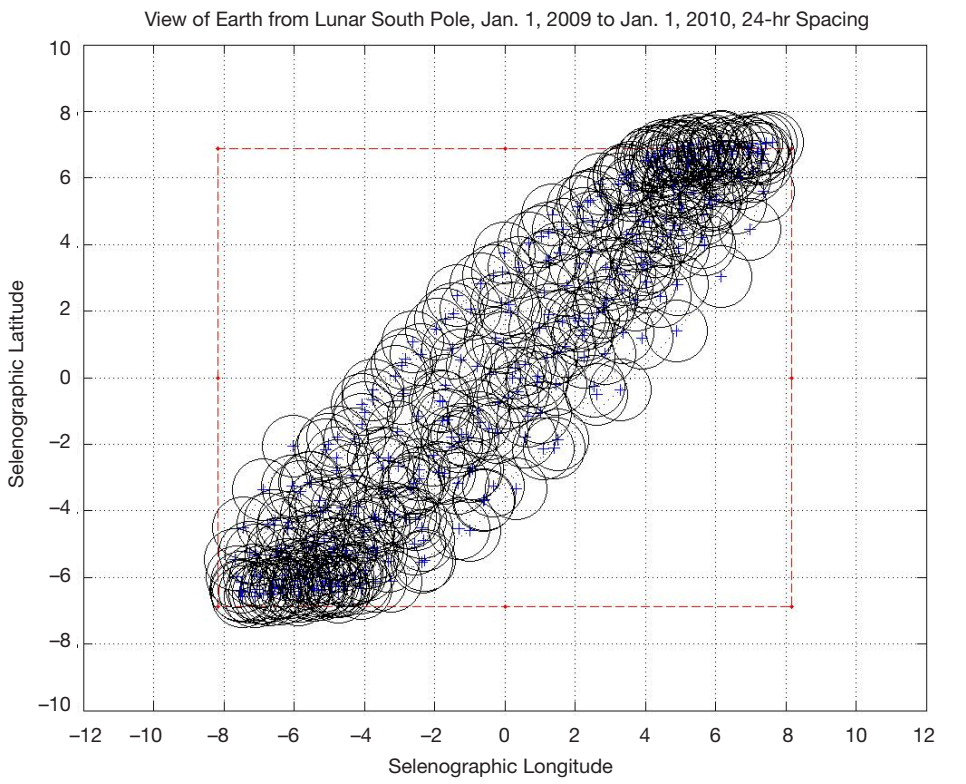


**Figure 9. Lunar south pole ephemeris data for Earth, 2009 to 2010.**

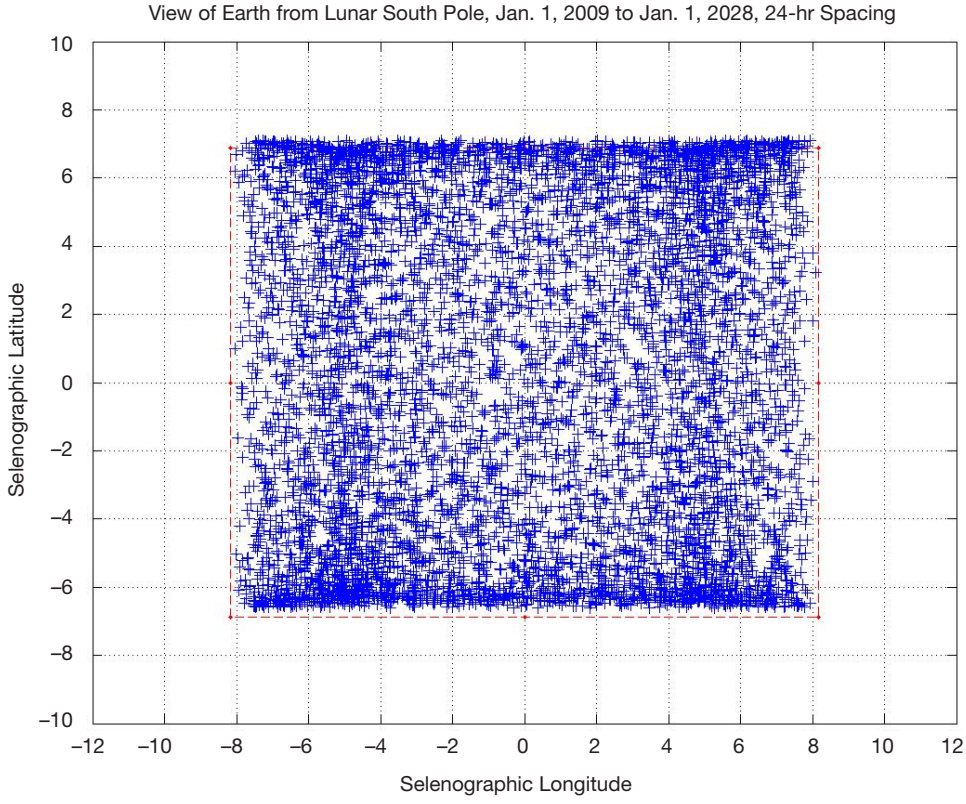


**Figure 10. Lunar south pole ephemeris data for Earth, 2009 to 2028.**

ing the lunar terrain. This 100 percent metric represents the percentage of the multiyear interval with full solar power available.

The three types of Earth illumination averages were computed in a similar way. The “0 percent of Earth visible” average integrated the horizon mask over the Earth bounding rectangle from -5.92 deg to +7.82 deg latitude. This metric requires that the horizon mask cover the entire Earth disk, up to Earth’s South Pole, to not count as visible to the lunar terrain. The 0-percent metric represents the percentage of the multiyear interval with some part of Earth visible at the tower height.

The “50 percent of Earth visible” average integrated the horizon mask over the Earth bounding rectangle from -6.87 deg to +6.87 deg latitude. This metric requires that the horizon mask cover half of Earth’s disk to not count as visible. This metric represents the amount of time that Earth’s southern hemisphere is visible.

The “100 percent of Earth visible” average integrated the horizon mask over the Earth bounding rectangle from -7.82 deg to +5.92 deg latitude. This metric requires that the horizon mask merely touch Earth’s disk at Earth’s North Pole, to not count as visible. This 100-percent metric represents the percentage of the multiyear interval with a full Earth visible at the tower height.

Additional metrics were estimated for solar power characterization (see Figure 6). The “months 100 percent visible” estimates the number of synodic months per year when the specified percentage of the solar disk is visible. It was computed by comparing the maximum horizon mask peak latitude to the upper and lower solar bounding rectangle limits. The fraction of the bounding rectangle above the maximum peak latitude represents the fraction of the year with continuous solar power.

The metric “days dark in winter month” lists the number of days during the lunar south pole winter with less than the specified percentage of solar disk visible. This was computed by finding the amount of each solar bounding rectangle lower edge that was below the horizon mask, normalizing with 360 deg, and multiplying by 29.5 days. For the “100 percent of solar disk visible” rectangle, this metric is approximately the sum of the number of days without full solar power during the winter synodic month. For the “0 percent of solar disk visible” metric, this is approximately the sum of the days without any solar light during the winter synodic month. This metric and the “days longest darkness” do not factor in possible solar eclipses, which can last up to 3.9 hr for a partial eclipse [5].

The metric “days longest darkness” is the longest continuous period with less than the specified percentage of solar disk visible. For the “100 percent of solar disk visible” value, this metric is the longest continuous period without full solar power. For the “0 percent of solar disk visible” value, this metric is the longest continuous period without any solar light.

The metrics “days dark in winter month” and “days longest darkness” can be used to set upper and lower bounds on the power system battery storage requirements. For a worst-case number that ignores recharge rates, battery storage can be based on the “days dark in winter

month” value associated with “100 percent of solar disk visible.” (Table 3 shows examples of these metrics.)

#### **IV. Results**

Results from the coarse (600-m resolution) horizon mask analysis were assembled in graphical and tabular formats. Contour plots for the lunar south pole region covered from X, Y = -129 km, -114 km to X, Y = +111 km, +126 km using 64 maps of size 30 km × 30 km. The combined maps show multiyear average solar illumination and Earth communications visibility values (see Figures 11 and 12). The boundaries for the coarse maps were chosen so that the entire Shackleton Crater fit within the coarse map from X, Y = -9 km, -24 km to X, Y = +21 km, +6 km. For the lunar north pole region, coarse maps cover from X, Y = -105 km, -105 km to X, Y = +105 km, +75 km. Figures 13 and 14 show multiyear average solar illumination and Earth communications visibility values.

For both lunar poles, sites with the most solar illumination were compared to illumination peak sites in the references. For the lunar south pole, coarse map sites with more than 80 percent average solar illumination were then examined with medium-resolution maps covering areas 2 km × 2 km. The medium-resolution maps were used to determine the size of each site across 40 m × 40 m pixels. The location of maximum solar illumination in X and Y was then determined for each site. These “peaks of illumination” were then examined with the fine horizon mask analysis to verify the illumination results and produce additional metrics.

##### **A. Coarse Horizon Mask Results**

For the south pole region, only five of the 64 coarse (30 km × 30 km) maps have peaks with more than 80 percent average solar illumination. These five maps cover the areas:

- (1) Shackleton Crater and the lunar south pole
- (2) The east ridge from Shackleton Crater
- (3) The west ridge from Shackleton Crater
- (4) The nearside–east rim of de Gerlache Crater
- (5) The nearside rim of de Gerlache Crater

Figure 15 shows the topographic elevation contours for Shackleton Crater. Figure 16 is the same area covered with solar and Earth illumination contours from the coarse horizon mask analysis. The solar illumination contours are every 10 percent and at 0.01 percent. Earth illumination contours are at 0.001, 10, 30, 50, 60, and 70 percent. The illumination data are for any part of the disk visible, or the “0 percent of solar/Earth disk visible” multi-year average illumination. Figures 17 through 24 are the same data for the remaining four coarse maps with peaks more than 80 percent average solar illumination.

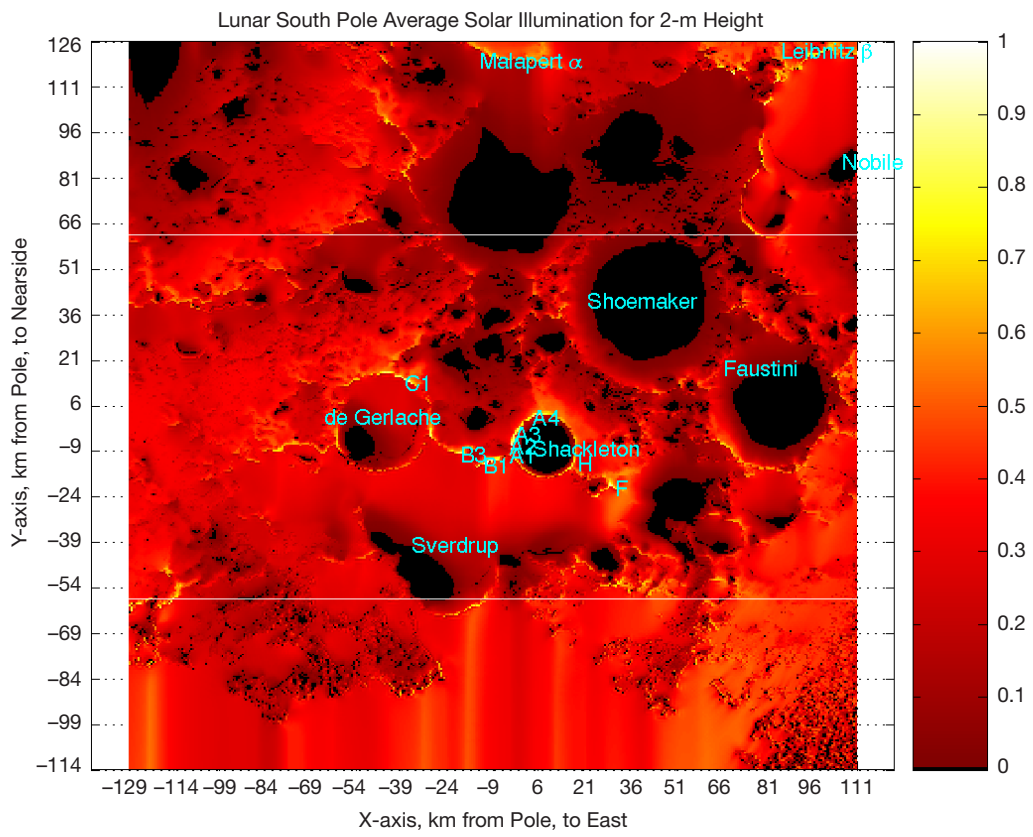


**Figure 11.** Lunar south pole solar illumination yearly average.

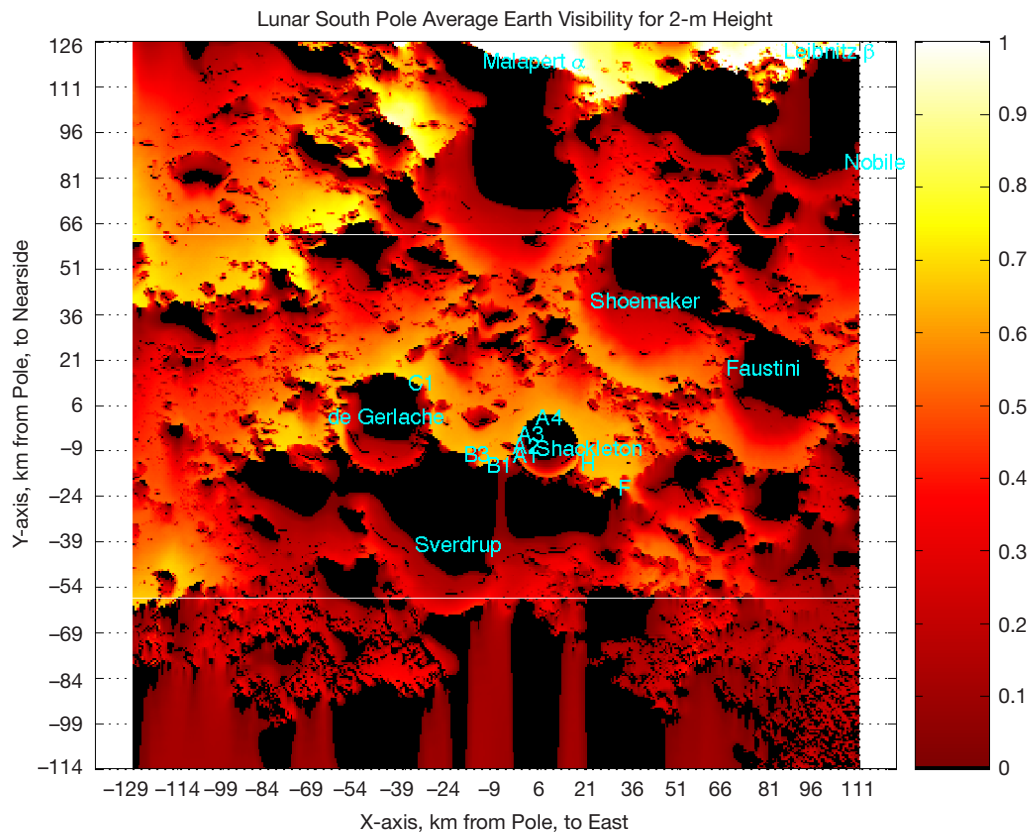


**Figure 12.** Lunar south pole DTE visibility yearly average.

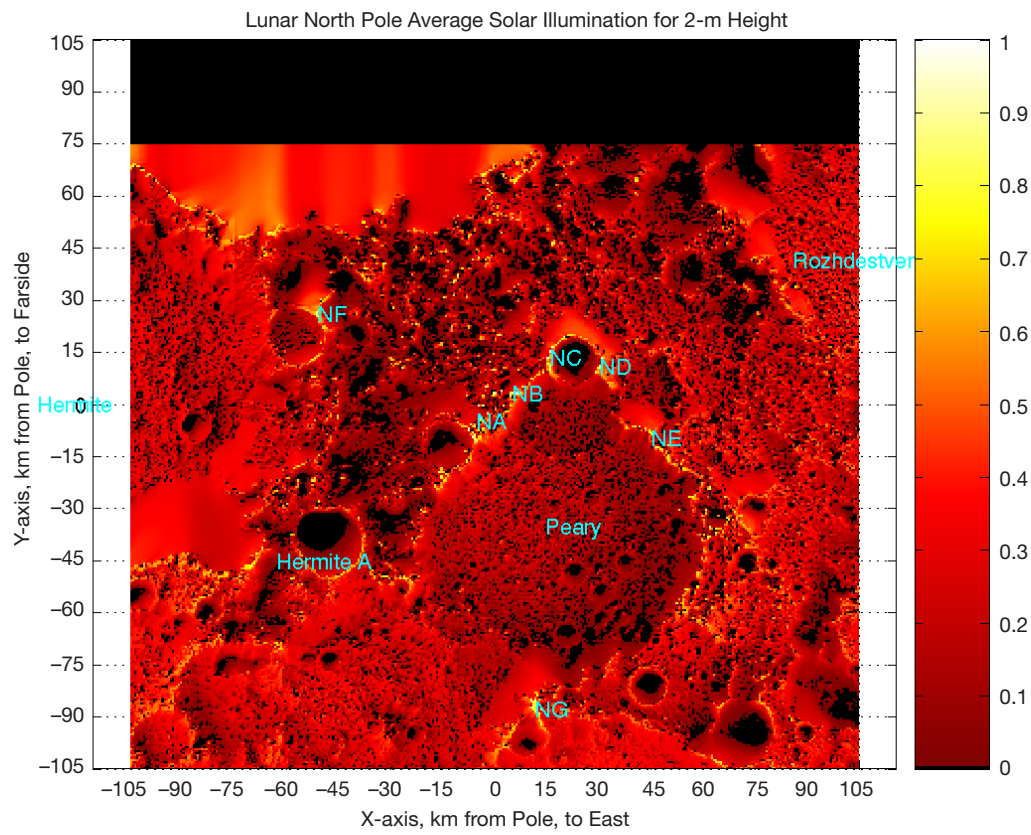


**Figure 13. Lunar north pole solar illumination yearly average.**

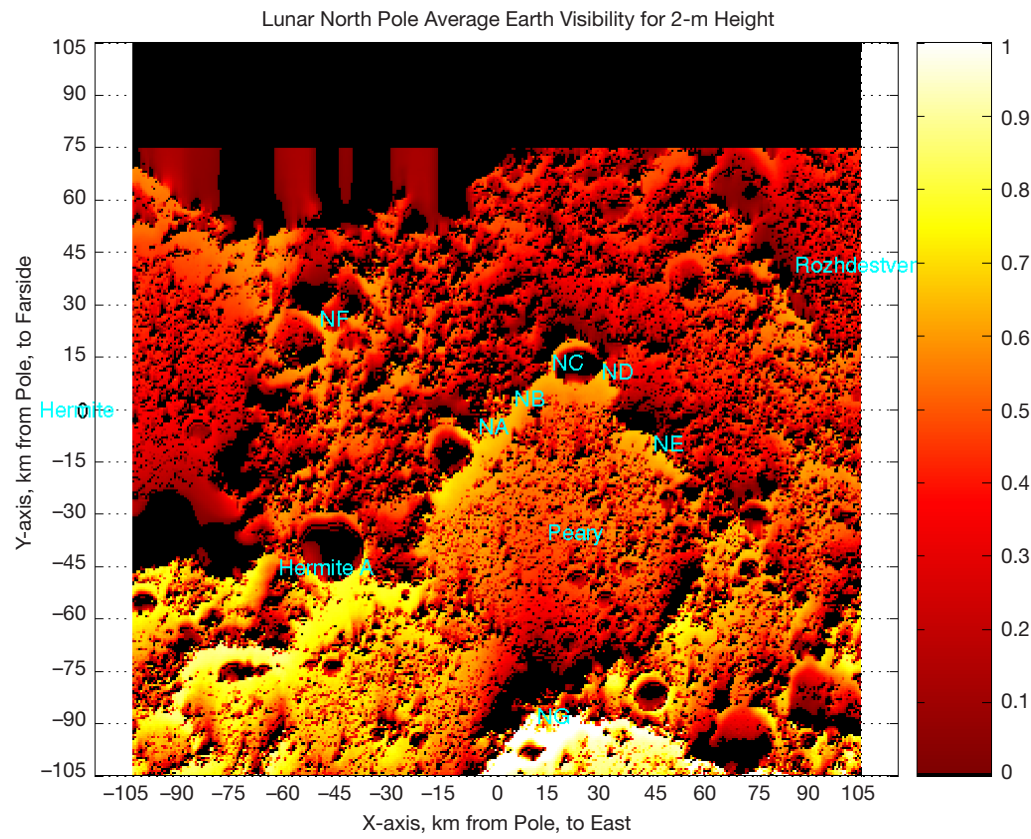


**Figure 14. Lunar north pole DTE visibility yearly average.**

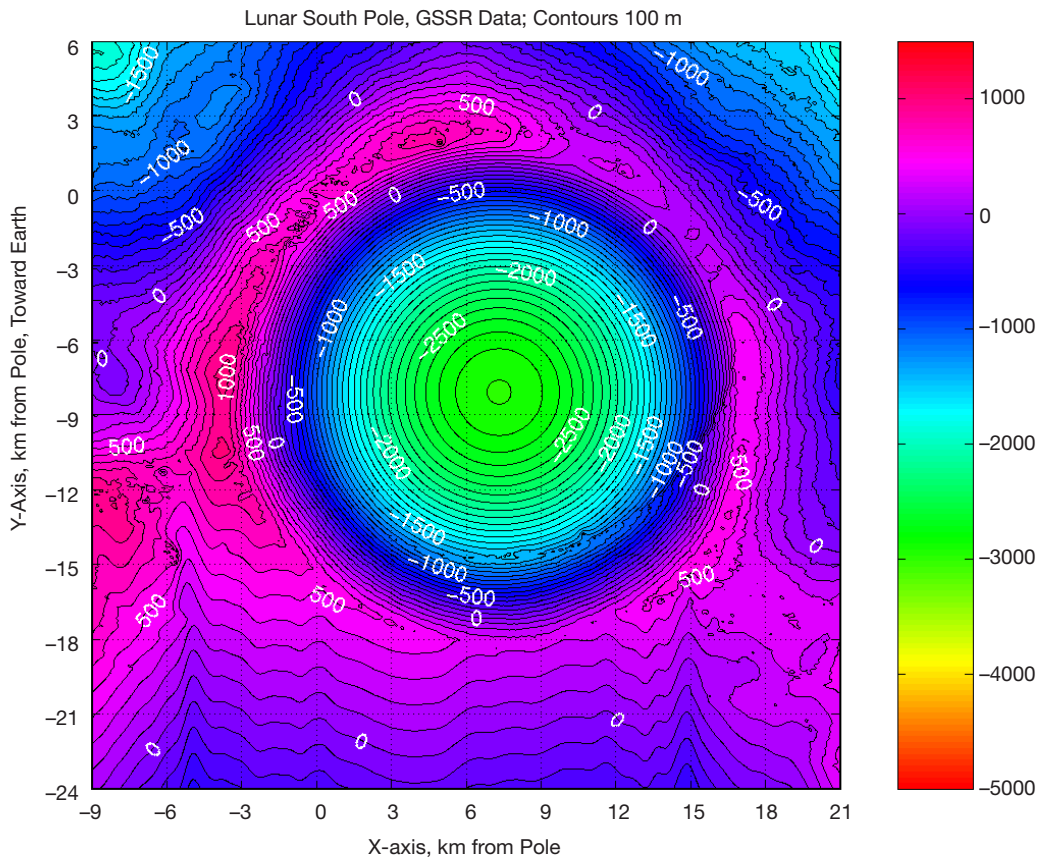


**Figure 15. Shackleton Crater elevation topography.**

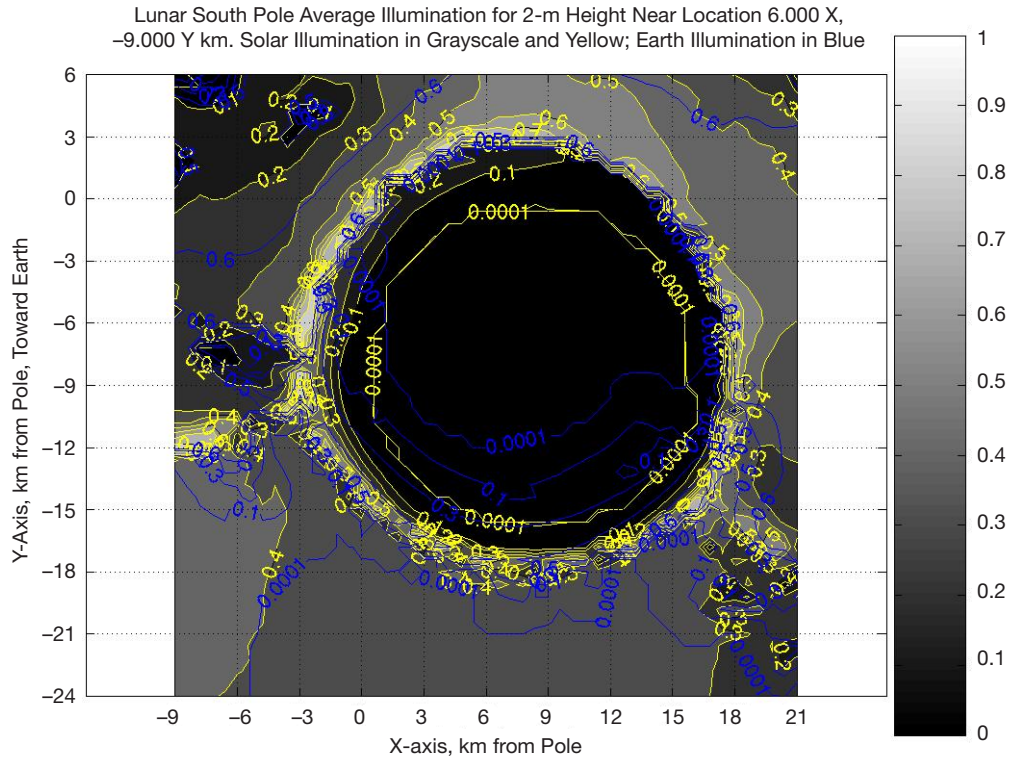


**Figure 16. Shackleton Crater yearly average illumination, coarse resolution.**

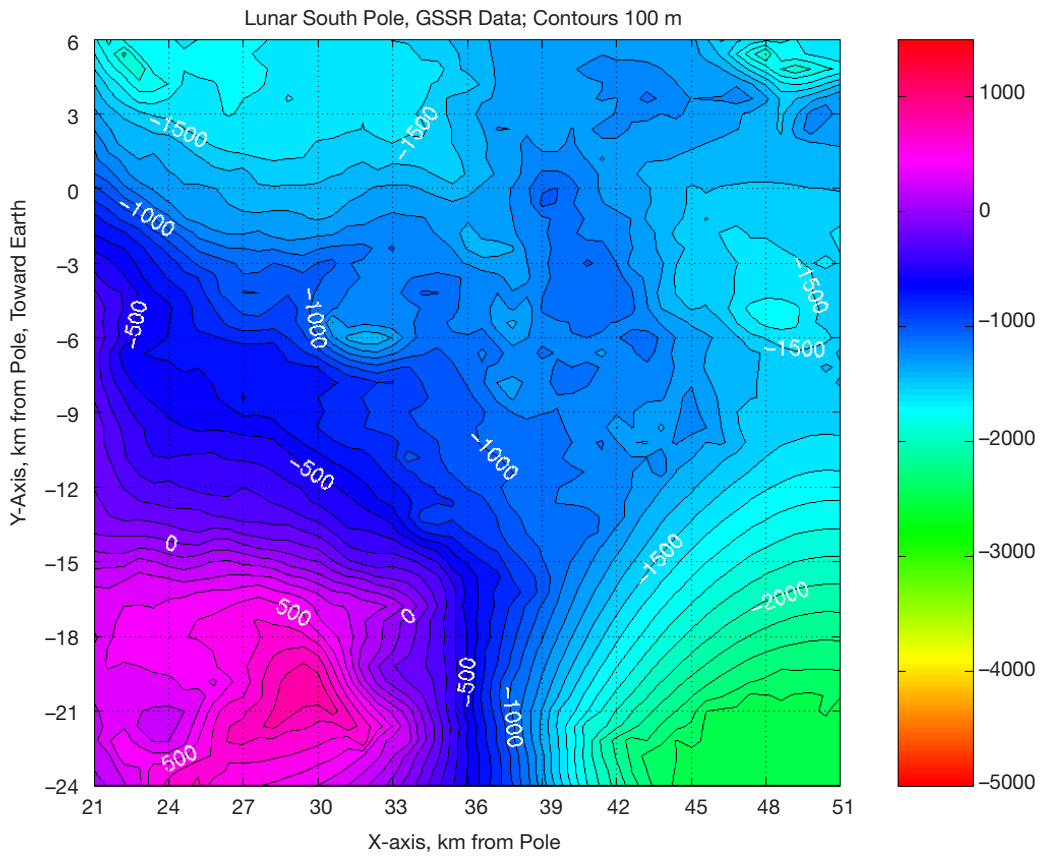


**Figure 17. Shackleton east ridge elevation topography.**

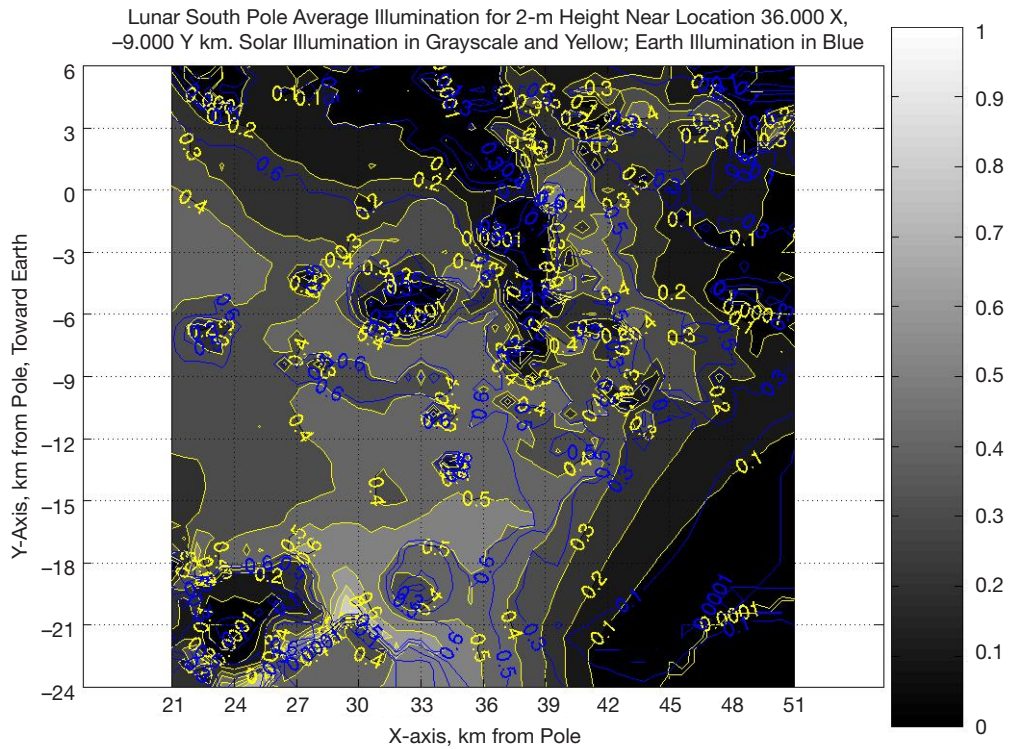


**Figure 18. Shackleton east ridge yearly average illumination, coarse resolution.**

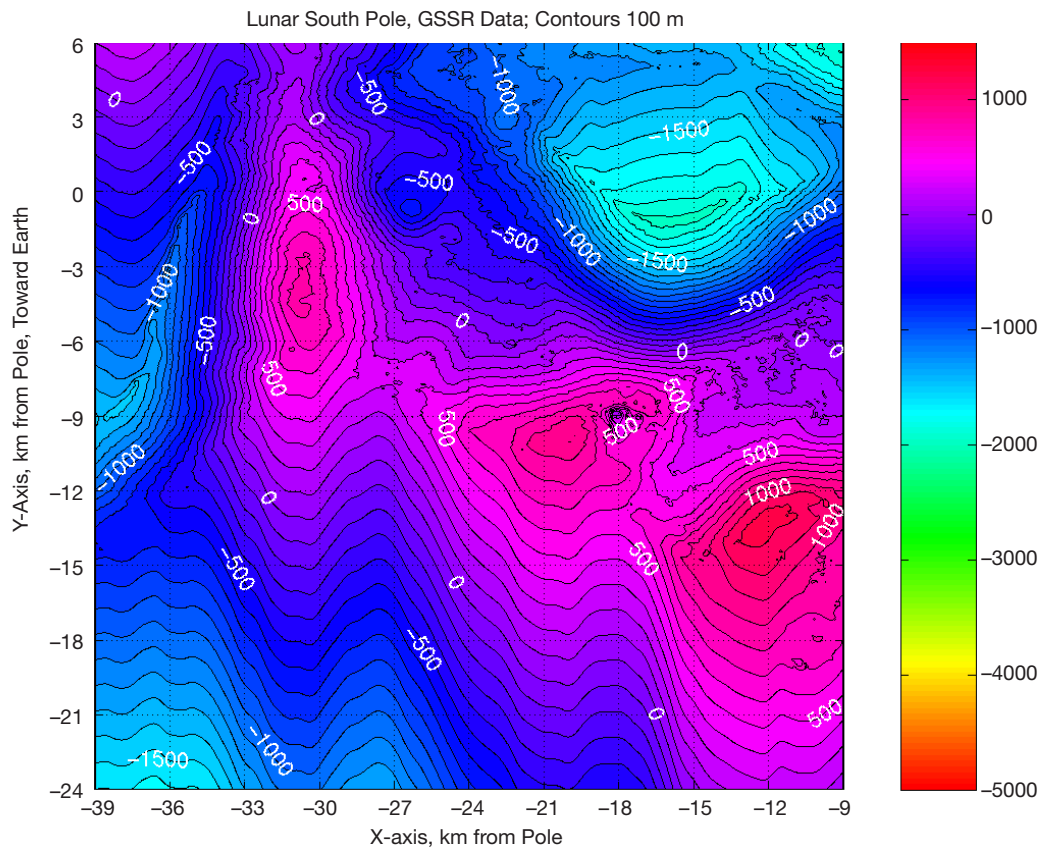


**Figure 19. Shackleton west ridge elevation topography.**

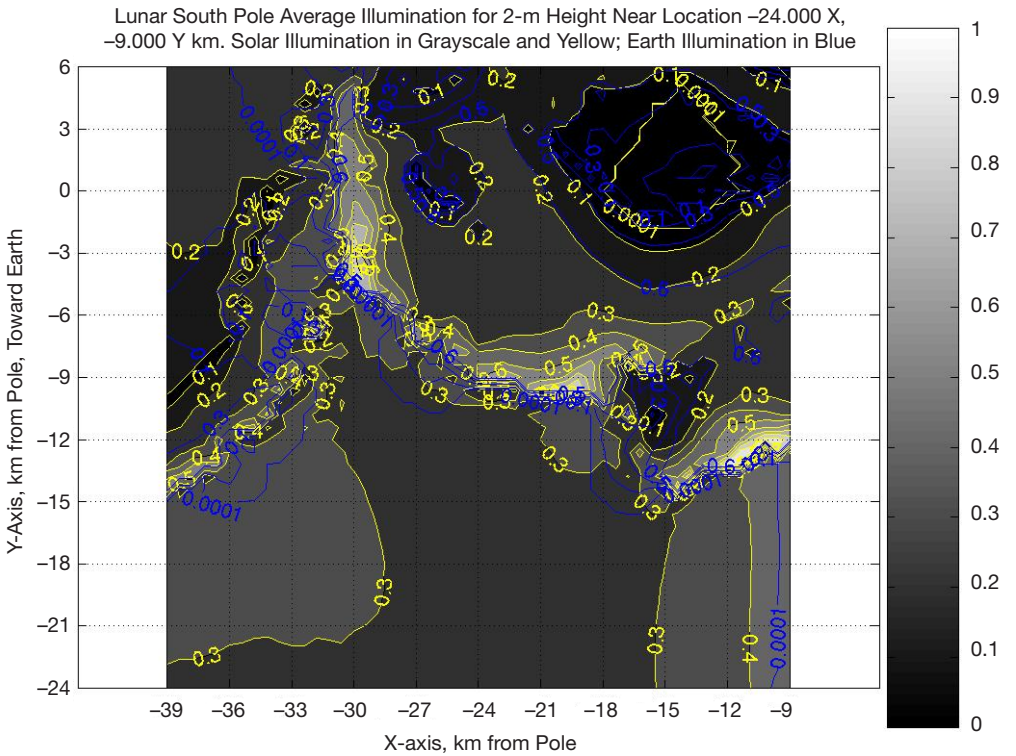


**Figure 20. Shackleton west ridge yearly average illumination, coarse resolution.**

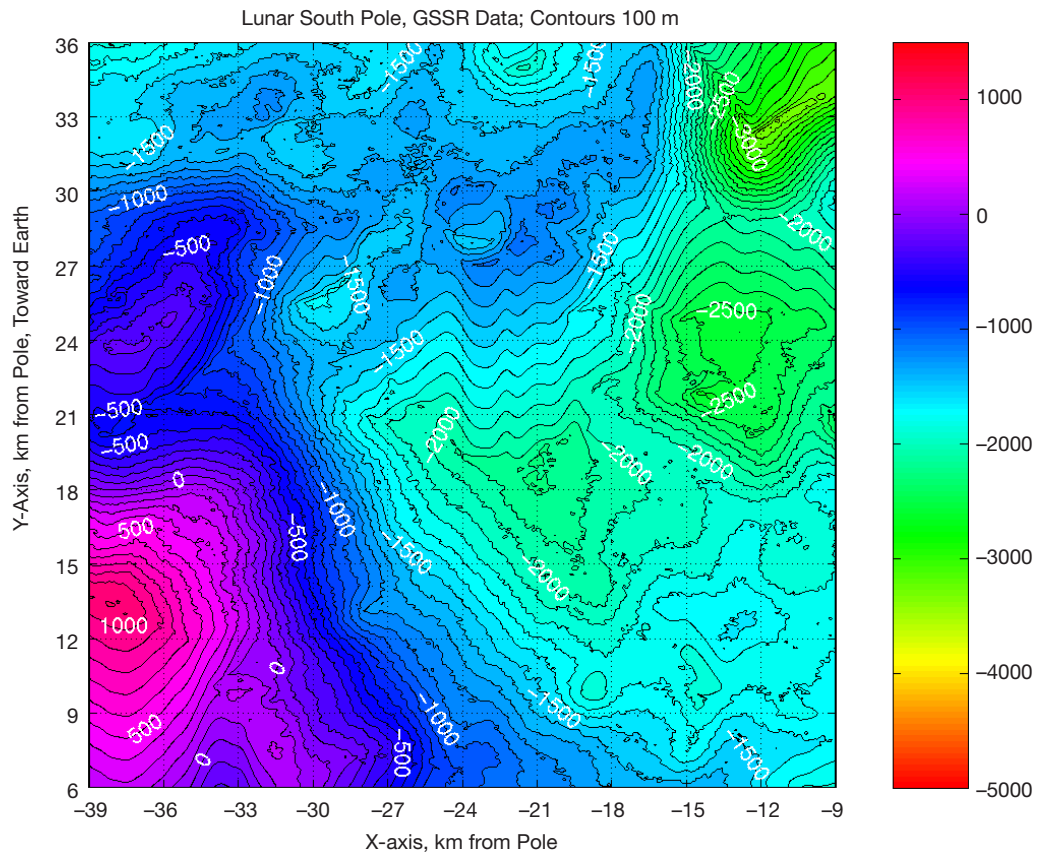


**Figure 21.** De Gerlache Crater nearside–east rim elevation topography.

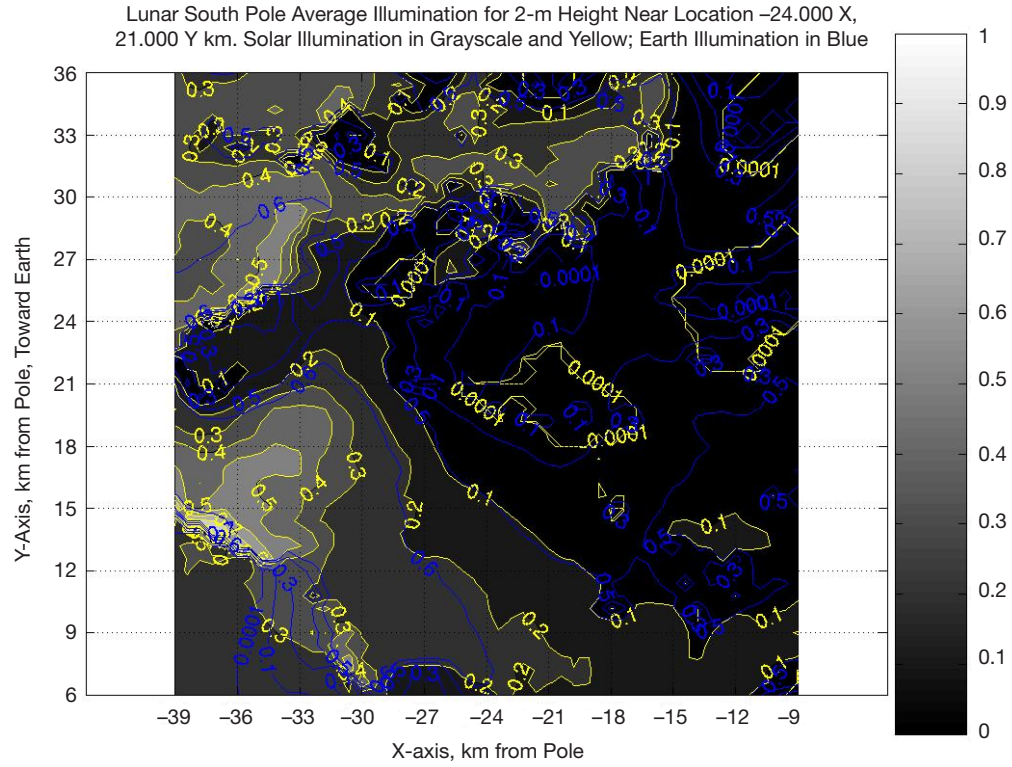


**Figure 22.** De Gerlache Crater nearside–east rim yearly average illumination, coarse resolution.

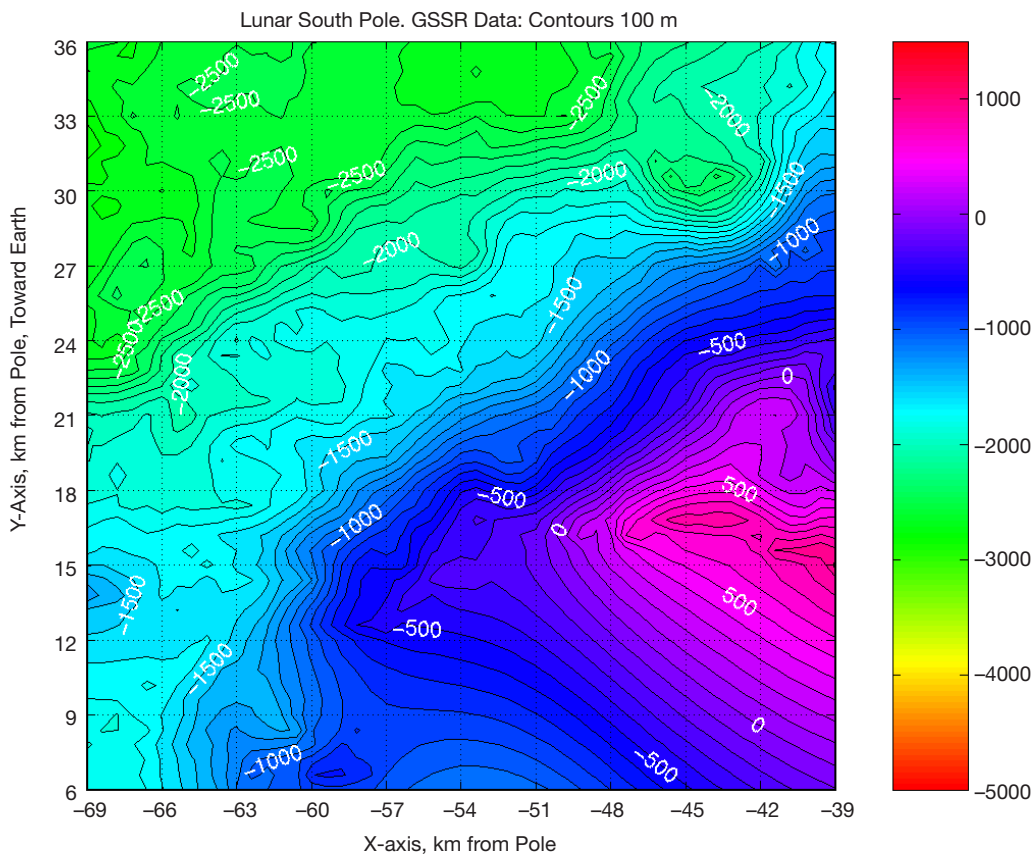


**Figure 23.** De Gerlache Crater nearside rim elevation topography.

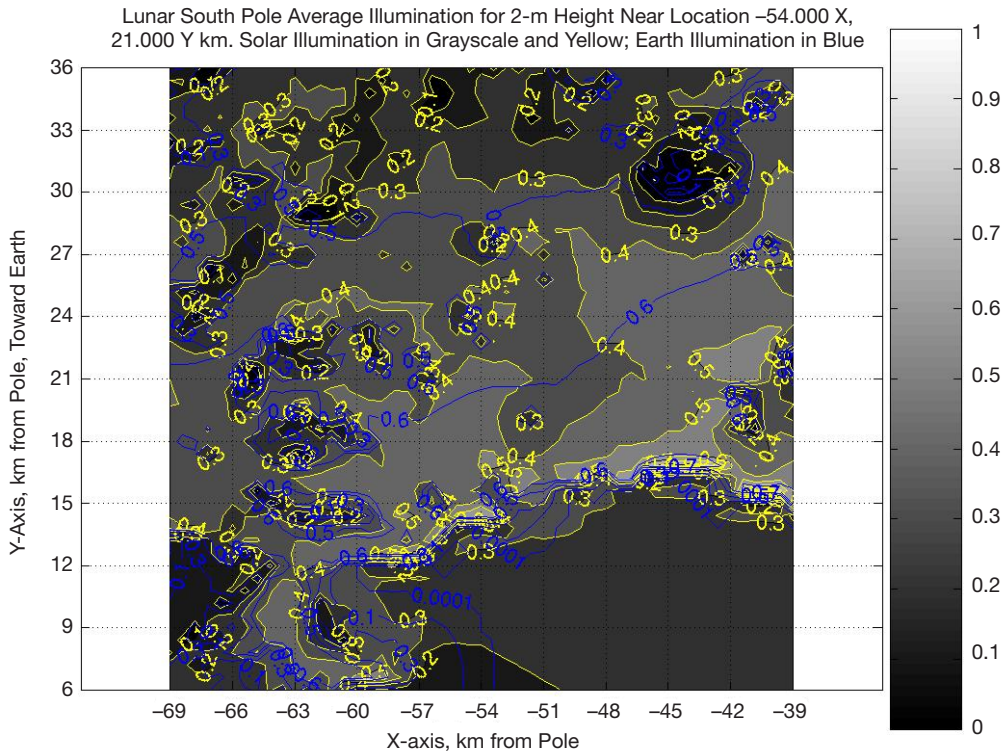


**Figure 24.** De Gerlache Crater nearside rim yearly average illumination, coarse resolution.

The maps confirm that most of Shackleton Crater is in permanent shadow (see Figures 11 and 16). The contours of the multiyear average solar illumination show small areas of maximum illumination on Shackleton Crater's rim and the west ridge. The maximum is around 90 percent of continuous illumination. The contours of Earth illumination show these same areas have a maximum multiyear average Earth visibility of about 60 percent. The figures also confirm the solar illumination peak sites identified in [3,4,5,6].

These five coarse maps were examined for points with multiyear average solar illumination peaks greater than 80 percent. Those points that are contiguous were given the same site peak name, matching the site names used in [4], Figure 1. Additional sites not listed in [4] are given the name of the closest site, followed by a new number; e.g., site B from [4] is listed here as sites B1, B2, and B3.

The site locations identified this way are shown in Figures 11 and 12. These sites show good correlation with the sites listed in [4], but are much lower in elevation due to the different DEM fitting method. Sites B1, A1, and A2 also match well with the three peaks of maximum solar illumination identified from Clementine images in [3].

Figures 13 and 14 show the north pole region. There are seven sites with multiyear average solar illumination peaks greater than 80 percent. These seven sites are marked NA through NG on the figures. The two best sites are NB and NC with multiyear average solar illumination above 95 percent. Site NG toward the lunar nearside has the highest multiyear average DTE communications of 96 percent.

#### B. Medium Horizon Mask Results

Based on the coarse map results, 31 medium-resolution maps were generated at 40-m resolution for the lunar south pole. These smaller  $2 \text{ km} \times 2 \text{ km}$  areas covered all the coarse map illumination peaks having greater than 80 percent multiyear average solar illumination. Locations in 17 of the 31 medium-resolution maps had multiyear average solar illumination peaks greater than 80 percent. Some solar illumination peaks that are likely DEM processing anomalies were not considered in the final analysis. Table 2 is a summary of the best multiyear average solar illumination peaks from the medium-resolution maps.

The two peaks with the highest multiyear average solar illumination are shown in Figures 25 through 28 in  $2 \text{ km} \times 2 \text{ km}$  maps. Figures 25 and 26 show the maximum for peak A1. Figure 25 shows the topographic elevation contours for the map centered on  $(-4, -10)$  on Shackleton Crater's west rim. Figure 26 is the same area covered with multiyear average solar illumination contours every 10 percent and at 0.01 percent. Figure 26 also shows multiyear average Earth illumination contours at 0.001, 10, 30, 50, 60, and 70 percent. The illumination data are for any part of the disk visible, or the "0 percent of solar/Earth disk visible" multiyear average illumination. Figures 27 and 28 show the multiyear average contours for peak B1.

**Table 2. Medium-view multiyear average solar illumination peaks selected for fine-resolution analysis.**

Map Center, X, Y km	Site Peak	X, km	Y, km	Latitude, deg	Longitude, deg	Elevation, m	Solar illumi- nation, %	Earth illumi- nation, %
-4, -10	A1	-3.72	-10.44	-89.633	-160.388	1071.74	95.58	62.49
-4, -8	A2	-3.68	-7.52	-89.723	-153.925	1050.05	94.20	63.89
-2, -4	A3	-2.20	-3.56	-89.861	-148.285	897.49	88.93	63.41
4, 2	A4	3.72	1.92	-89.861	62.700	896.57	91.46	63.99
-12, -14	B1	-12.40	-13.68	-89.388	-137.810	1260.93	97.52	65.10
-20, -10	B3	-19.96	-10.04	-89.260	-116.703	1003.61	88.63	65.52
16, -14	H	16.52	-13.08	-89.302	128.371	631.43	84.22	64.89
	C1	-38.24	13.40	-88.657	-70.688	1143.8		
	F	28.76	-21.36	-88.813	126.601	947.4		
Malapert $\alpha$ , MA		3.56	119.60	-86.037	1.704	4206.8		
Leibnitz $\beta$ , LB		101.32	123.04	-84.722	39.470	6054.5		

The following conclusions resulted from examining these illumination peaks and the multi-year average solar illumination and DTE maps:

- (1) The multiyear average solar illumination maximums occur on the highest peak in the map areas. This is expected, since taller peaks have the least-obstructed views of the Sun.
- (2) At 40-m resolution, the data show several grid points next to each illumination maximum peak with nearly the same multiyear average solar illumination value. This implies the peaks are spread over several pixels. This could also happen because the DEM data set was made self-consistent by smoothing.
- (3) Within a 2 km  $\times$  2 km area, there can be several small peaks with greater than 80 percent multiyear average solar illumination. An area hundreds of meters across may surround the actual maximum peak that also has nearly 80 percent multiyear average solar illumination.
- (4) Multiyear average Earth visibility is also maximized on the highest peaks in the site.
- (5) Small changes in the terrain slope (as shown in the topographic maps) greatly reduce the multiyear average solar illumination, even within hundreds of meters of the solar maximum peaks. This implies that finding solar maximum peaks using spacecraft pictures of illuminated terrain may be problematic. The conditions may mix light and dark terrain pixels in spacecraft pictures, even during the mid-summer days. This also indicates that the solar maximum peaks may not be visible on photographs due to shallow Sun angles.
- (6) The highest site within a region will have the greatest multiyear average solar illumination. For instance, site B1 and B3 are located on two broad plateaus about 8 km apart, but site B1 is about 300 m higher, and has significantly higher multi-year average solar illumination.

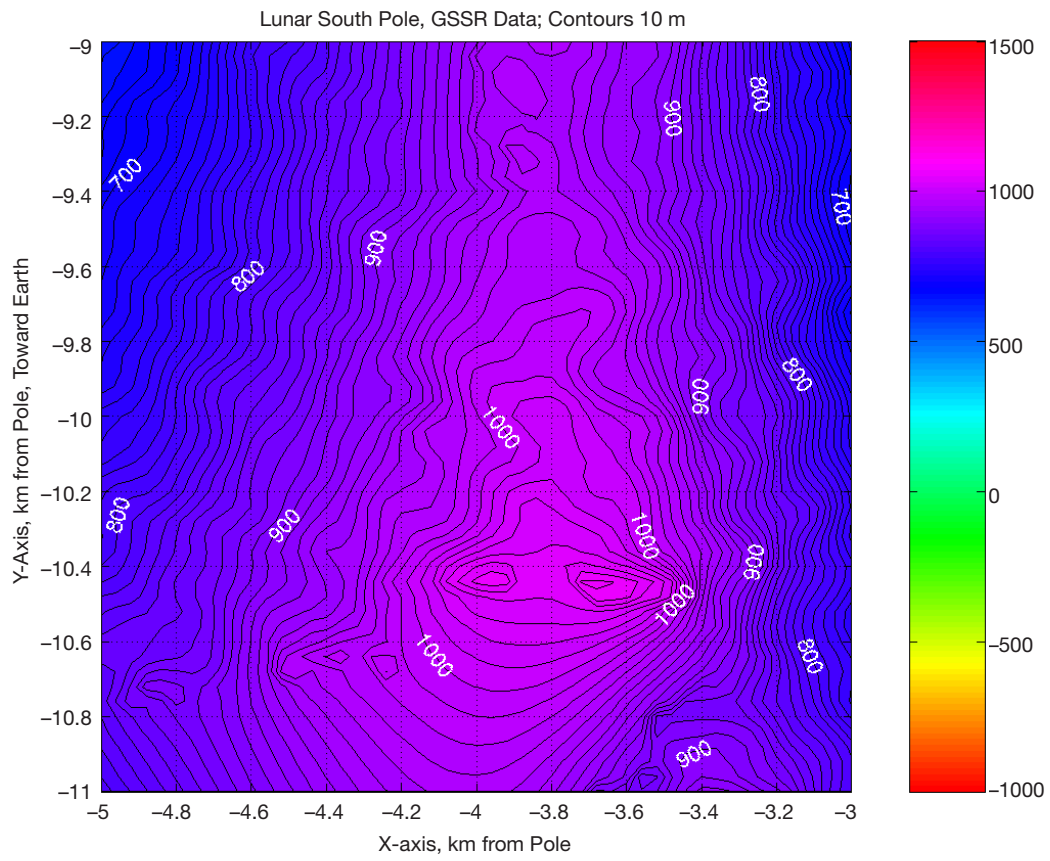


**Figure 25. Site A1 elevation topography.**

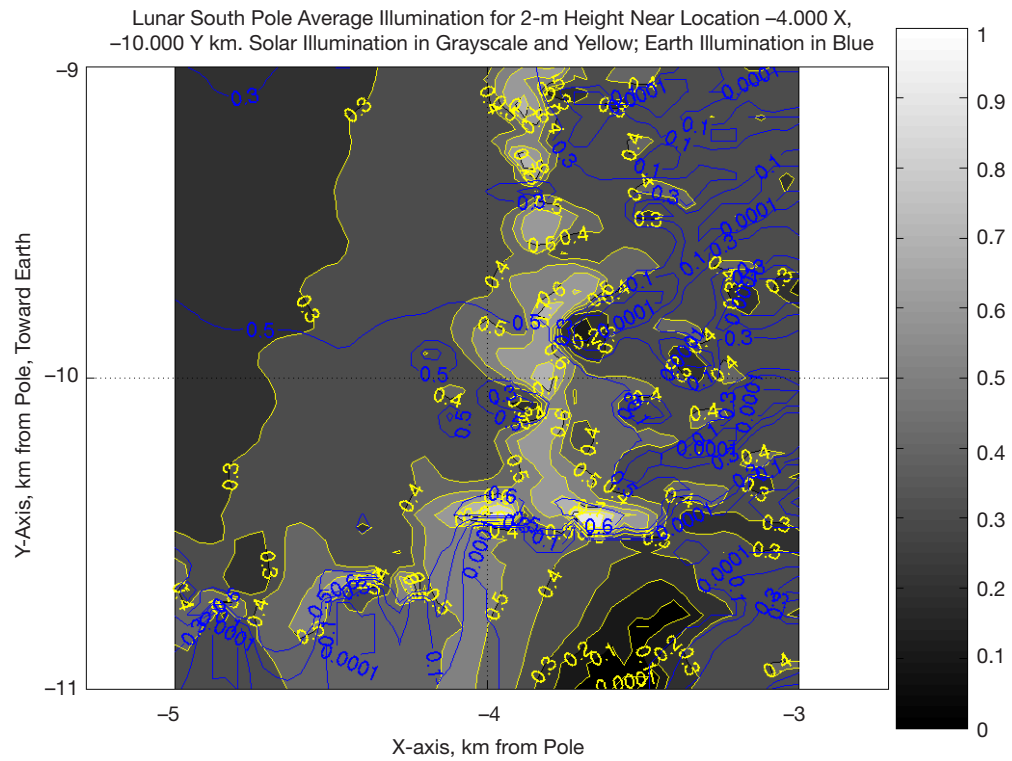


**Figure 26. Site A1 yearly average illumination, medium resolution.**

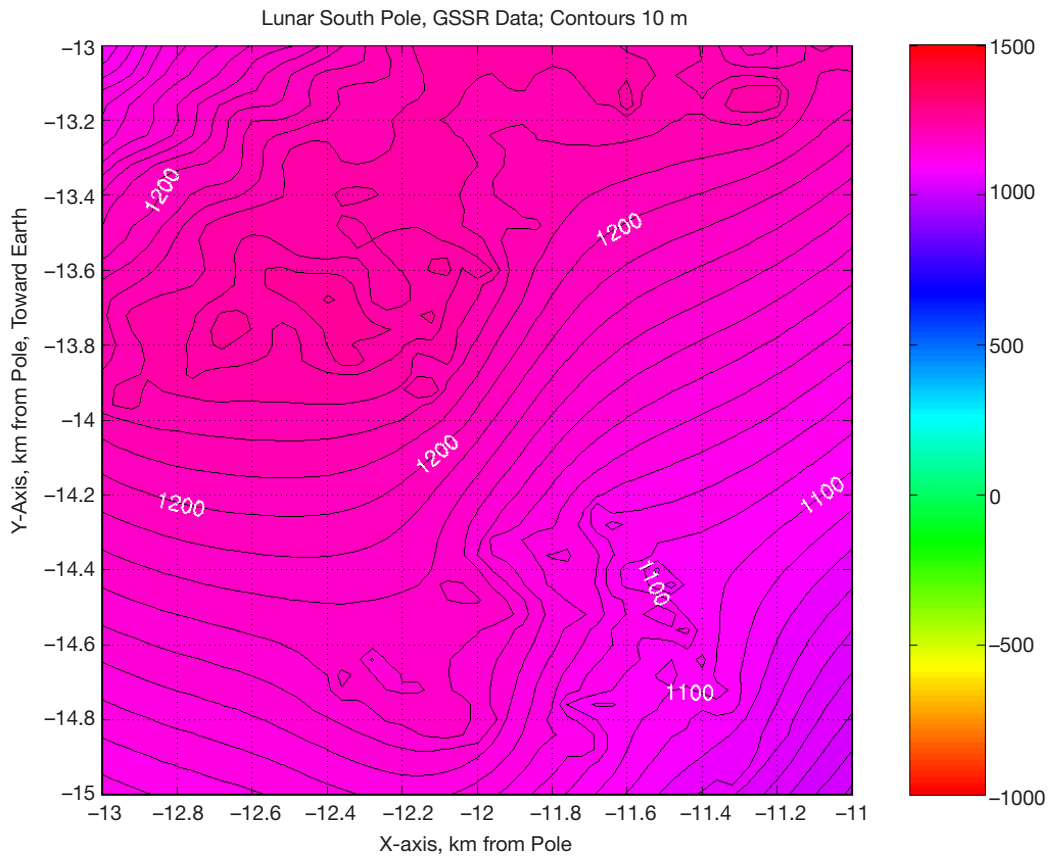


**Figure 27. Site B1 elevation topography.**

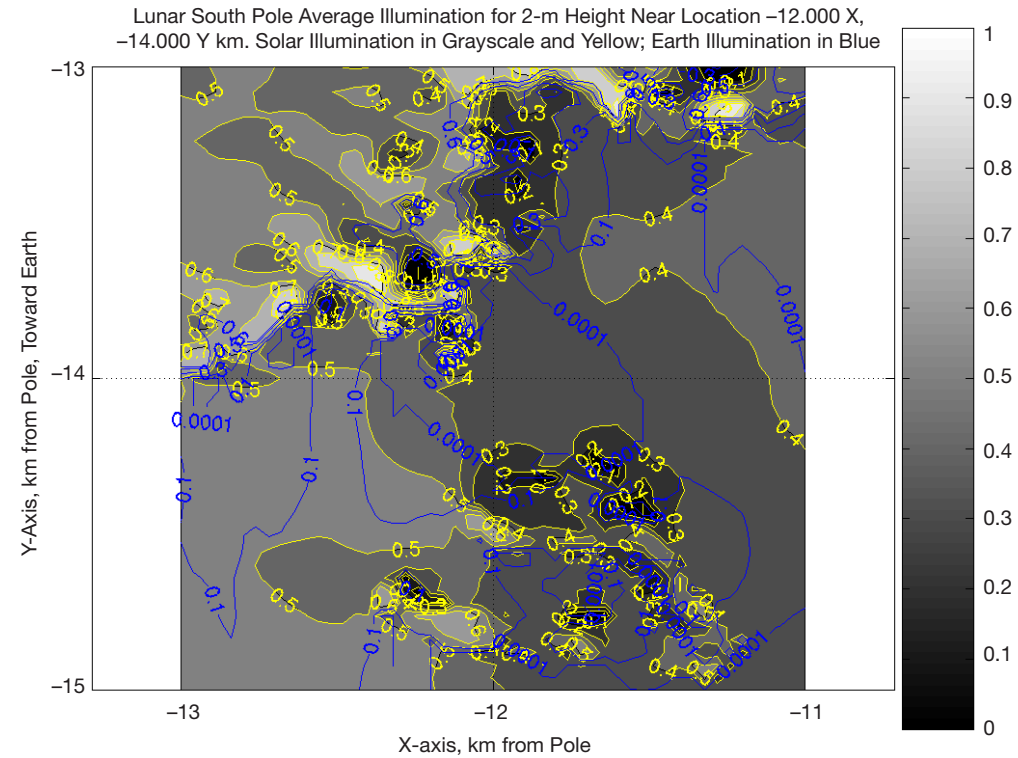


**Figure 28. Site B1 yearly average illumination, medium resolution.**

Based on these observations, sites C1 and F from [4] deserved further investigation. The peaks of the two tallest mountains near the pole (Malapert  $\alpha$  and Leibnitz  $\beta$ ) were also added to the list, as sites MA and LB. The coarse-map peaks that were labeled site B2 and a processing artifact peak near A4 were dropped from consideration. A fine-resolution horizon mask was computed for the highest elevation point of each site in Table 2.

### C. Fine Horizon Mask Results

Fine-resolution horizon masks were computed for 11 site locations in the lunar south pole region. Based on the coarse map results, four site locations from the lunar north pole were added to the fine-resolution analysis list. The results for the 15 sites are shown in Tables 3 and 4.

The sites A1, A2, and B1 have the highest multiyear average solar illumination for the lunar south pole sites. The other southern peaks do not have solar illumination metrics as good as these three peaks, primarily because of lower elevation. Site C1 is higher than sites A1 and A2, but is much farther from the south pole and therefore gets less average solar illumination.

The lunar north pole fine-resolution analysis used the same azimuth resolution as the lunar south pole analysis (1-deg steps), but was performed using 600-m resolution data. The four northern sites in Tables 2 and 3 are sites NA, NB, NC, and NG. The sites NB and NC have higher multiyear average solar illumination than the lunar south pole sites, primarily because there are no obscuring peaks as tall as Malapert  $\alpha$  and Leibnitz  $\beta$  at the lunar north pole.

At the lunar south pole, site B1 has the highest average yearly solar illumination of 97 percent. Site B1 also has an average Earth visibility (65 percent) higher than the nearby sites A1 through A4. Site B1 has the most months of continuous solar illumination, with some part of the solar disk visible during 8 synodic months. The solar power generation metrics show that site B1 has the lowest total days of darkness, during the winter month, for these five sites. However, sites A1 and A2 have shorter total days of continuous darkness, during the winter month, than site B1. This could be significant when selecting the base locations, since it directly affects the battery storage sizing for the base.

These solar illumination statistics are for multiyear averages of the solar motion. This allows valid site-to-site comparisons, but doesn't provide information for the solar illumination on specific dates.

The multiyear average Earth visibility metrics of Table 4 indicate little variation between the sites on the rim of Shackleton Crater. In general, the best visibility to some part of the Earth is around 65 percent for the lunar polar regions. From these peaks, the entire Earth is visible about 50 percent of the sidereal month. Therefore, continuous polar lunar base coverage requires some kind of Earth relay. The sites on the peaks of Malapert  $\alpha$  and Leibnitz  $\beta$  have 100 percent visibility of Earth at all times. These sites also have direct line of sight to

**Table 3. Fine-resolution solar illumination statistics.**

Site	X, km	Y, km	Multiyear Average Illumination			Months 100% Visible			Days Dark in Winter Month			Days Longest Continuous Darkness		
			(0)	(50)	(100)	(0)	(50)	(100)	(0)	(50)	(100)	(0)	(50)	(100)
A1	-3.720	-10.440	93.46	90.36	86.31	4.05	2.98	1.92	8.94	12.06	15.99	2.46	2.71	5.50
A2	-3.680	-7.520	92.98	89.47	84.83	4.46	3.40	2.34	10.58	13.70	18.29	2.63	2.79	3.04
A3	-2.200	-3.560	85.36	80.75	75.22	0.05	0.00	0.00	14.03	18.37	20.43	4.92	8.86	9.19
A4	3.720	1.910	87.83	83.66	78.51	0.00	0.00	0.00	13.21	17.06	19.85	6.23	7.63	9.92
B1	-12.400	-13.680	97.01	94.79	91.67	8.02	6.96	5.90	6.32	9.59	11.73	2.79	4.10	7.54
B3	-19.960	-10.040	83.84	80.50	76.55	0.00	0.00	0.00	11.56	14.19	16.07	6.89	7.05	10.09
H	16.520	-13.080	77.53	72.20	66.57	1.60	0.53	0.00	17.39	18.95	19.85	10.42	10.74	13.78
C1	-38.240	13.400	90.01	86.95	83.12	4.29	3.23	2.17	9.27	12.22	13.94	5.33	5.90	11.31
F	28.760	-21.360	89.28	85.97	81.77	4.13	3.06	2.00	10.09	12.87	15.25	5.90	6.39	8.94
MA	3.560	119.600	82.08	78.36	74.49	0.88	0.00	0.00	12.62	12.86	13.93	12.62	12.86	13.18
LB	101.320	123.040	79.06	77.43	75.82	0.00	0.00	0.00	9.15	9.48	9.72	9.15	9.48	9.72
NA	-7.800	-7.200	94.52	89.83	83.70	5.46	4.39	3.33	12.88	18.70	23.79	3.69	12.14	12.30
NB	4.200	2.400	97.51	94.01	88.11	7.39	6.33	5.27	8.12	15.67	23.38	3.12	4.92	6.23
NC	15.000	13.200	98.36	96.19	92.73	8.99	7.93	6.87	5.58	8.94	15.34	1.56	3.61	8.77
NG	12.600	-89.400	86.56	83.16	79.64	4.44	3.37	2.31	11.39	11.80	12.37	11.39	11.80	12.29

**Table 4. Fine-resolution Earth visibility statistics.**

Site	X, km	Y, km	Multiyear Average DTE Communications		
			(0)	(50)	(100)
A1	-3.720	-10.440	62.20	55.29	48.37
A2	-3.680	-7.520	63.90	56.98	50.07
A3	-2.200	-3.560	63.41	56.50	49.58
A4	3.720	1.910	63.97	57.06	50.14
B1	-12.400	-13.680	65.16	58.24	51.33
B3	-19.960	-10.040	65.60	58.69	51.77
H	16.520	-13.080	62.02	55.11	48.20
C1	-38.240	13.400	70.97	64.05	57.14
F	28.760	-21.360	67.30	60.38	53.47
MA	3.560	119.600	100.00	100.00	94.68
LB	101.320	123.040	100.00	100.00	100.00
NA	-7.800	-7.200	70.82	63.91	57.00
NB	4.200	2.400	66.89	59.98	53.07
NC	15.000	13.200	66.18	59.27	52.35
NG	12.600	-89.400	96.15	91.62	85.37

the rim of Shackleton Crater. This makes possible a communications system design using a radio frequency reflector at one of these sites as a continuous relay between Earth and sites on the rim of Shackleton Crater. For the lunar north pole, site NG on the north rim of Peary Crater has 96 percent visibility of Earth. This site could provide a nearly continuous relay between Earth and sites NB and NC near the lunar south pole.

#### D. Computing Metrics from Ephemeris Data

The validity of assuming a uniform distribution of solar and Earth exposure was investigated using actual ephemeris data. The location of the Sun and Earth were computed using the HORIZONS ephemeris computation service<sup>6</sup> provided by JPL. Data files were created in selenographic latitude and longitude for the period January 1, 2009, to January 1, 2028, with 24-hr spacing. This period covered a complete 18.6-yr regression of the longitude of the ascending node of the Moon. Ephemeris data were generated for four observation data sets:

- (1) The view of the Sun from the lunar north pole
- (2) The view of the Sun from the lunar south pole
- (3) The view of Earth from the lunar north pole
- (4) The view of Earth from the lunar south pole

These data were used to compute four distribution patterns in selenographic latitude and longitude. The distribution patterns show the time in hours each location is covered by the Sun (or Earth) during the 19-yr period. Figures 29 and 30 show the Sun distribution patterns as seen from the lunar north and south poles. Figures 31 and 32 show the Earth distribution patterns as seen from the lunar north and south poles. The figures show that the distribution pattern is not uniform. The Sun distributions are uniform in longitude and vary less than a factor of 2 from the average in latitude. The Earth distributions are approximately uniform in longitude between + and -4 deg latitude. The Earth distribution does have four peaks almost 3.7 times the average value, but these peaks are at greater than + and -5 deg latitude. For site locations at the lunar poles, the four Earth distribution peaks are located so that two peaks are always visible, and two peaks are always below the horizon. This effectively cancels out the asymmetry of the Earth distribution patterns as seen from the lunar poles.

These distribution patterns were computed using the following algorithms. Starting with the first set of latitude, longitude, and time ( $lat_i$ ,  $long_i$ ,  $t_i$ ) in an ephemeris file; compute the angular distance and time between the current point and next point with the equation

$$L = \sqrt{(long_{i+1} - long_i)^2 + (lat_{i+1} - lat_i)^2} \quad (1)$$

$$T = t_{i+1} - t_i$$

---

<sup>6</sup> <http://ssd.jpl.nasa.gov/?horizons>

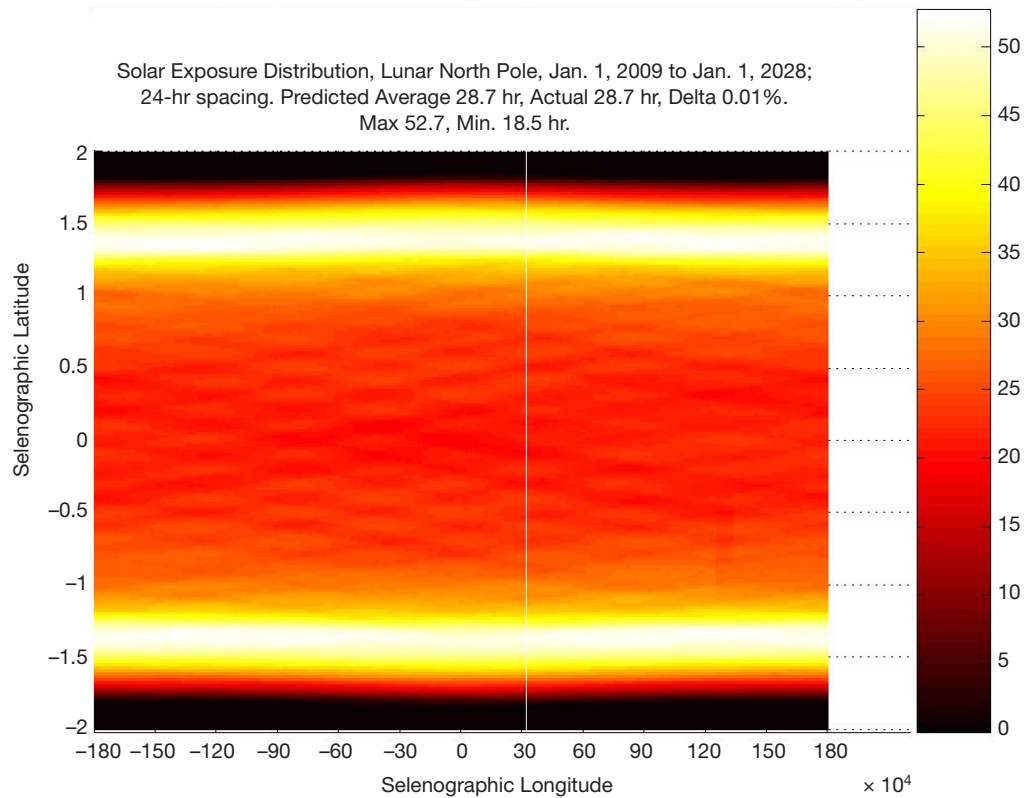


**Figure 29. Solar distribution pattern, viewed from the lunar north pole.**

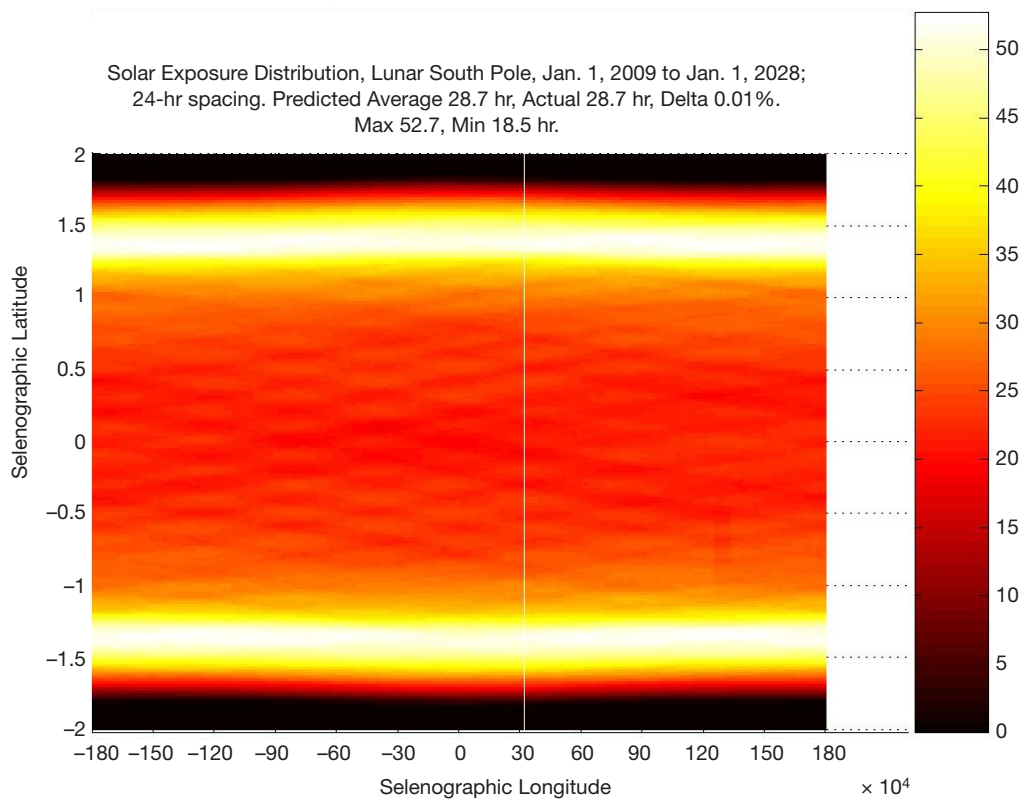


**Figure 30. Solar distribution pattern, viewed from the lunar south pole.**

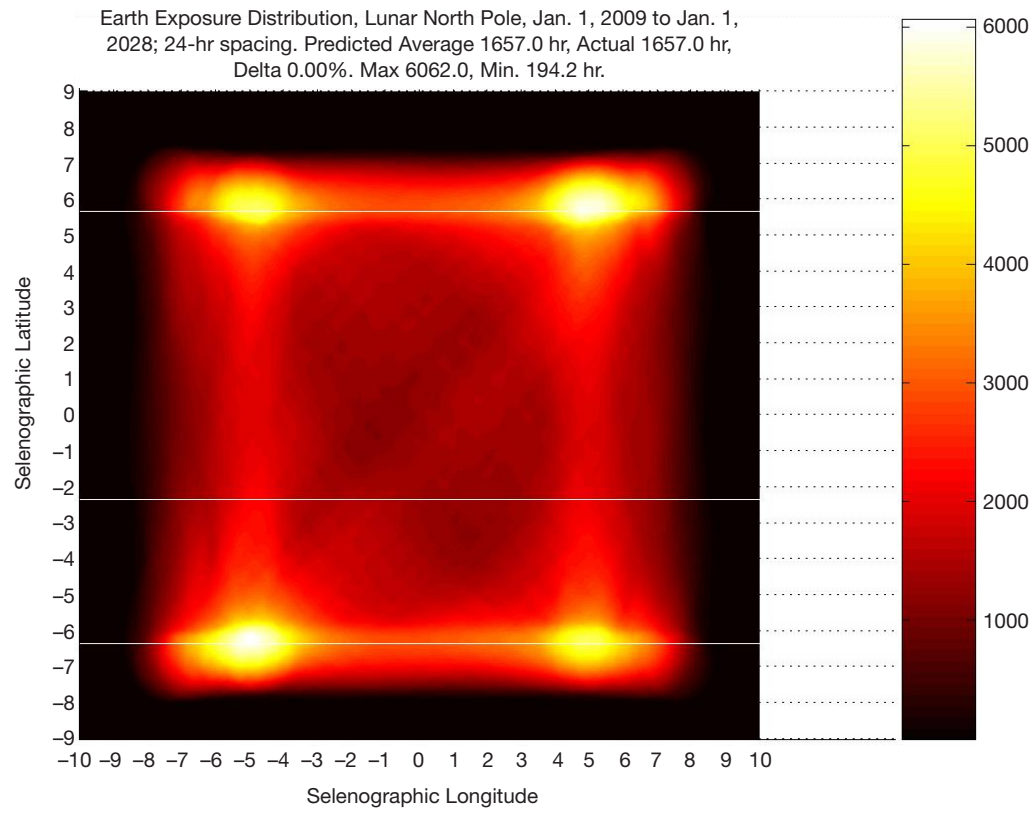


**Figure 31. Earth distribution pattern, viewed from the lunar north pole.**

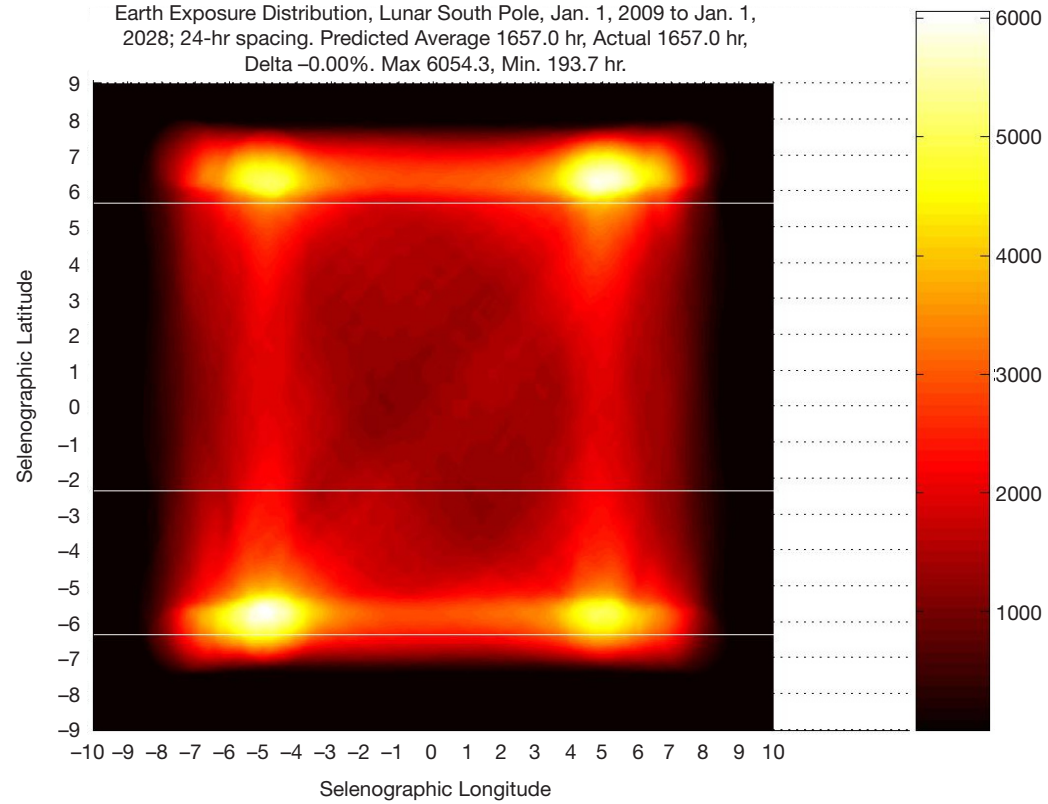


**Figure 32. Earth distribution pattern, viewed from the lunar south pole.**

For each point ( $\text{lat}$ ,  $\text{long}$ ) within  $R$  (0.95 deg for Earth, 0.25 deg for the Sun) of the line between  $(\text{lat}_i, \text{long}_i, t_i)$  and  $(\text{lat}_{i+1}, \text{long}_{i+1}, t_{i+1})$ , perform a coordinate transformation that maps  $(\text{lat}, \text{long})$  to  $(Y_i, X_i)$  and  $(Y_{i+1}, X_{i+1})$ . The coordinate  $X_i$  is the distance from  $(\text{lat}_i, \text{long}_i)$  along the line  $L$  between  $(\text{lat}_i, \text{long}_i)$  and  $(\text{lat}_{i+1}, \text{long}_{i+1})$ . The coordinate  $Y_i$  is the perpendicular from the line  $L$ . The coordinate  $X_{i+1}$  is the distance from  $(\text{lat}_{i+1}, \text{long}_{i+1})$  along the line  $L$  and  $Y_{i+1}$  is the perpendicular from the line  $L$ . The transformation is given by

$$\begin{aligned} X_i &= \left\{ (\text{long} - \text{long}_i) \frac{(\text{long}_{i+1} - \text{long}_i)}{L} + (\text{lat} - \text{lat}_i) \frac{(\text{lat}_{i+1} - \text{lat}_i)}{L} \right\} \\ Y_i &= \left\{ (\text{lat} - \text{lat}_i) \frac{(\text{long}_{i+1} - \text{long}_i)}{L} - (\text{long} - \text{long}_i) \frac{(\text{lat}_{i+1} - \text{lat}_i)}{L} \right\} \\ X_{i+1} &= L - X_i \\ Y_{i+1} &= Y_i \end{aligned} \quad (2)$$

The exposure time,  $E$ , at each point  $(\text{lat}, \text{long})$  that gets added to the distribution pattern for the ephemeris point  $(\text{lat}_i, \text{long}_i, t_i)$  is determined by the region the transformed coordinates  $(Y_i, X_i)$  and  $(Y_{i+1}, X_{i+1})$  occupy. The five regions are given by

- [1],  $(X_i^2 + Y_i^2 < R^2)$  and  $(X_{i+1}^2 + Y_{i+1}^2 < R^2) \Rightarrow E = T$
- [2], Not in [1] and  $(X_i^2 + Y_i^2 < R^2) \Rightarrow E = \frac{T}{L}(X_i + \sqrt{R^2 - Y_i^2})$
- [3], Not in [1] and  $(X_{i+1}^2 + Y_{i+1}^2 < R^2) \Rightarrow E = \frac{T}{L}(X_{i+1} + \sqrt{R^2 - Y_{i+1}^2})$
- [4], Not in [2][3] and  $(Y_i < R)$  and  $(X_i > 0)$  and  $(X_i < L) \Rightarrow E = \frac{2T}{L}\sqrt{R^2 - Y_i^2}$
- [5], Not in [2][3][4]  $\Rightarrow E = 0$

The summation of  $E$  over all the points  $(\text{lat}, \text{long})$  for each data point in an ephemeris file produced a distribution pattern for the time interval of the ephemeris. The results from the four ephemeris data sets were used to produce Figures 29 through 32. The distribution pattern was also used in place of the original uniform distribution to produce new fine-resolution metrics as described in Section III.D. The ephemeris distributions were used to compute the fine-resolution metrics shown in blue in Figures 6, 33, 34, 35, and 36 for the lunar pole sites B1, C1, MA, NC, and NG. The metrics show an agreement better than 5 percent between the metrics based on a uniform distribution and the metrics based on the ephemeris distribution from 2009 to 2028.

#### E. Using Towers to Improve Metrics

Solar illumination and Earth visibility metrics increase with increased altitude above the local terrain. The following equations show this variation as a function of altitude and distance from the pole. The equations assume a spherical lunar surface of radius,  $R$ , an altitude above this surface,  $h$ , and a distance from the pole,  $d$ . The equations are written in terms of colatitude,  $\theta$ , and below-the-horizon view angle,  $\phi$ , given by the following equations:

$$\theta = \frac{d}{R} \times \frac{180}{\pi} \quad (4)$$

$$\phi = \arccos\left(\frac{R}{R+h}\right) \quad (5)$$

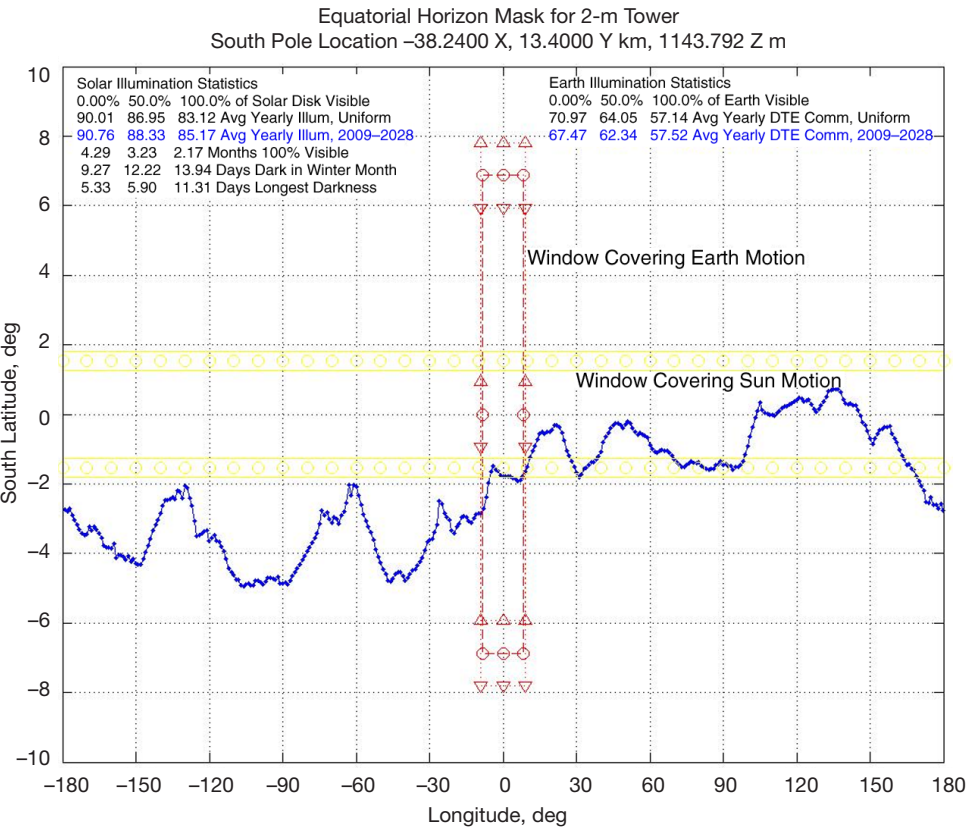


Figure 33. Site C1 terrain horizon mask with 1-deg azimuth spacing, in selenographic coordinates.

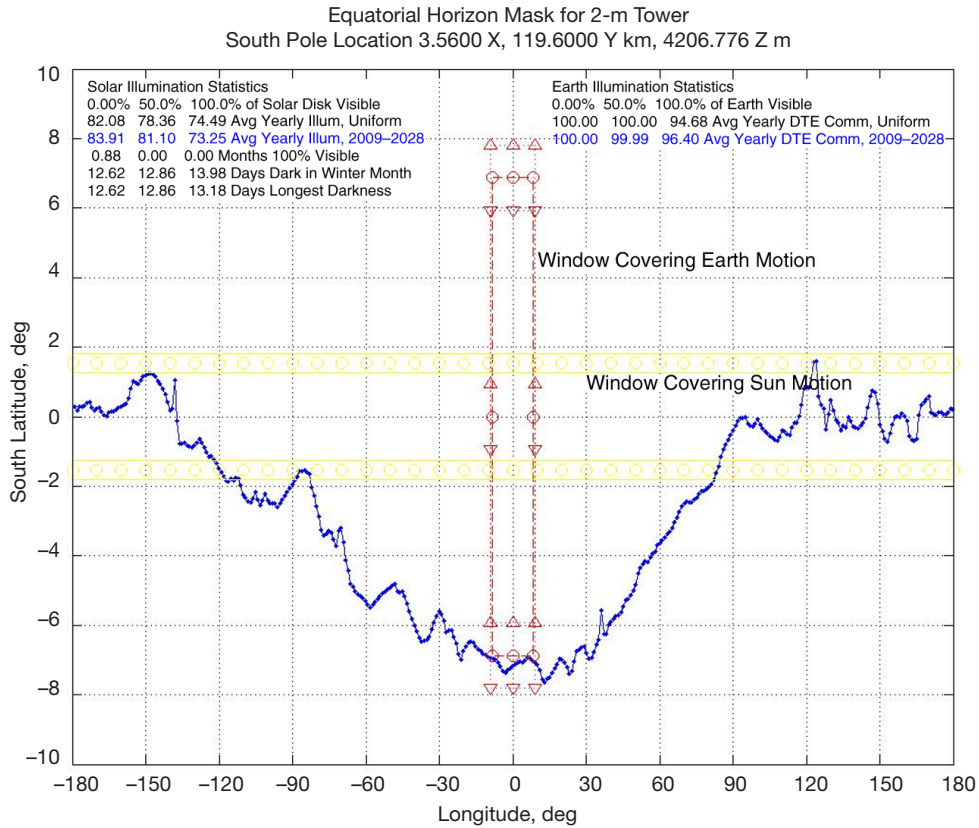


Figure 34. Site MA terrain horizon mask with 1-deg azimuth spacing, in selenographic coordinates.

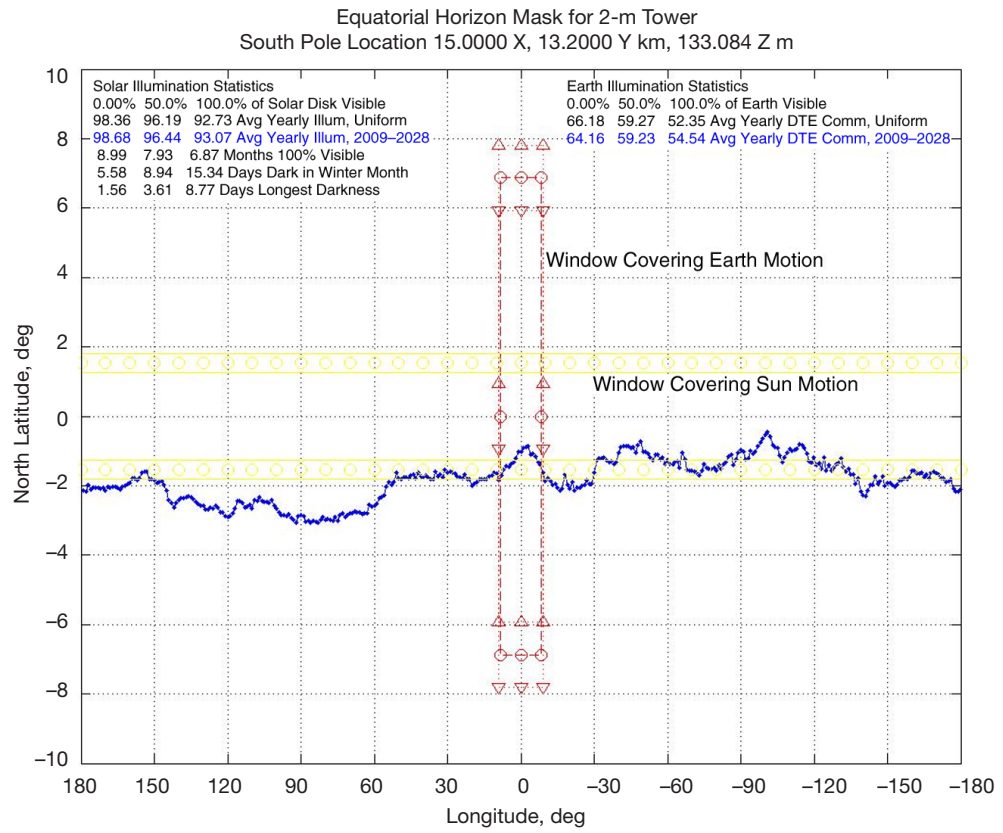


Figure 35. Site NC terrain horizon mask with 1-deg azimuth spacing, in selenographic coordinates.

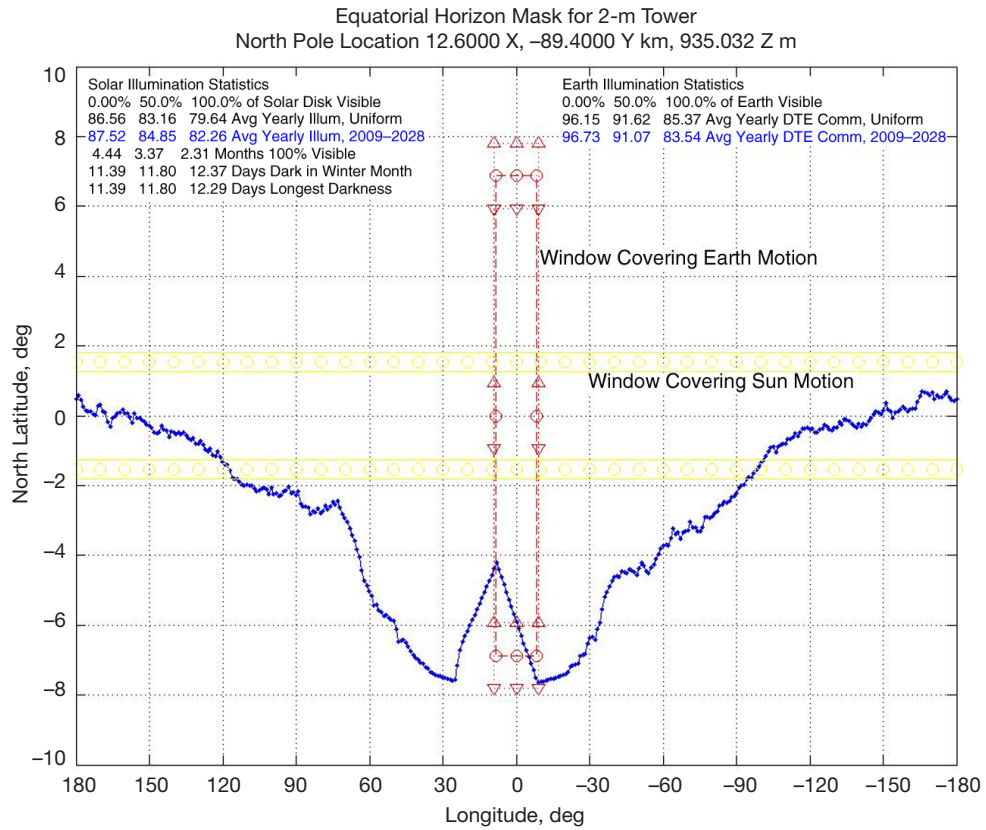


Figure 36. Site NG terrain horizon mask, with 1-deg azimuth spacing, in selenographic coordinates.

The multiyear average equations integrate along the local horizon, converted to lunar latitude-longitude coordinates. The derivation uses an approximation for small angles that gives Equation (7). This equation is valid for small angles near the polar regions.

$$\begin{aligned} \text{longitude} &\approx \arccos\left(\frac{-\phi - \text{latitude}}{\theta}\right) \\ \text{latitude} &\approx -\phi - \theta \cos(\text{longitude}) \end{aligned} \quad (6)$$

Integrating the area above the horizon mask and between the solar latitude limits produced an equation for the yearly average solar illumination. The solar latitude limits are + and  $-1.54$  degrees, represented by + and  $-\alpha$  below. The equation uses the variables  $L1$  for the longitude where the horizon mask crosses  $-\alpha$  latitude, and  $L2$  for the longitude where the horizon mask crosses  $+\alpha$  latitude. These variables are

$$\begin{aligned} L1 &= \begin{cases} \text{if } (\theta + \phi) \geq \alpha, & \arccos\left(\frac{-\phi + \alpha}{\theta}\right) \\ \text{else,} & 0 \end{cases} \\ L2 &= \begin{cases} \text{if } (\theta - \phi) \geq \alpha, & \arccos\left(\frac{-\phi - \alpha}{\theta}\right) \\ \text{else,} & 180 \end{cases} \end{aligned} \quad (7)$$

The multiyear average solar illumination,  $I$ , is then predicted by the equation:

$$I = \frac{L1}{180} + \frac{(\alpha + \phi)(L2 - L1)}{360 \times \alpha} + \frac{\theta}{2\pi\alpha} [\sin(L2) - \sin(L1)] \quad (8)$$

Integrating the area above the horizon mask and between the Earth latitude limits produced the multiyear average DTE communication equation. The Earth latitude limits are + and  $-6.87$  deg, represented by + and  $-\gamma$  below. The Earth longitude limits of + and  $-8.16$  deg are represented by + and  $-\beta$  below. The equation uses the variable  $L0$  for the longitude of the site at Cartesian coordinates  $(x,y)$  centered on the pole. The equation uses the variable  $L1$  for the longitude where the horizon mask crosses  $-\beta$  latitude. These variables are given by

$$\begin{aligned} L0 &= \text{abs}[\arctan(x/y)] \\ L1 &= \begin{cases} \text{if } (\theta + \phi) \geq \gamma, & \arccos\left(\frac{-\phi + \gamma}{\theta}\right) - L0 \\ \text{else,} & -\beta \end{cases} \end{aligned} \quad (9)$$

The yearly average Earth communications, DTE, is then given by the equation

$$DTE = \frac{1}{4\gamma\beta} \left\{ 2\gamma(L1 + \beta) + (\gamma + \phi)(\beta - L1) + \theta \frac{180}{\pi} [\sin(\beta + L0) - \sin(L1 + L0)] \right\} \quad (10)$$

Comparing these theoretical equations with the computed illumination and DTE communications averages required using an adjusted lunar reference altitude at the poles. The lunar reference geoid radius of 1738 km is not a good average value for the terrain at either pole. The lunar south pole is part of the Aitken Basin, and the GSSR DEM elevations have an average of  $-1880$  m within 200 km of the south pole. The lunar north pole region has an average elevation of  $-1673$  m within 150 km of the north pole. These averages were

subtracted from base site reference altitude to get the value of  $h$  used in Equation (2). This effectively gives the base sites a higher elevation relative to the local average elevation.

For selected base sites, solar illumination and DTE communications averages were computed for tower heights from 2 m to 1500 m, and in some cases 3000 m. Fine-resolution metrics were produced from the assumed uniform Sun and Earth distributions and from the distribution patterns produced from the 2009 to 2028 ephemeris data.

Table 5 shows multiyear average metrics for site B1 near the lunar south pole at ( $X, Y$ ) location ( $-12.400 X \text{ km}$ ,  $-13.680 Y \text{ km}$ ) and elevation 1261 m. The table shows metrics for tower heights from 2 m to 3000 m above the base surface elevation.

Table 6 shows the multiyear average metrics for a uniform Earth distribution and the actual Earth distribution pattern produced from the 2009 to 2028 ephemeris data.

For the two distribution patterns, the same solar illumination metric agrees within 1 percent and the same Earth visibility metric agrees within 5 percent. This level of agreement validates the simplifying assumption of uniform Sun and Earth distributions over the bounding latitude and longitude regions.

These tower heights, plus adjusted altitudes and base locations, were used in Equations (4) through (10) to get predicted values of the multiyear average metrics. The results are shown in Figures 37 and 38. Figure 37 shows the black curves of Equation (8) plotted parametrically with distance from the pole. For the selected sites, the computed multiyear average solar illumination (assuming a uniform distribution) is shown by squares, connected by a dashed line with the theoretical yearly average for the same location and tower heights.

**Table 5. Solar illumination metrics for site B1 tower heights.**

Tower height, m	Solar Illumination Statistics, Assumed Uniform Distribution			Solar Illumination Statistics, Distribution from 2009 to 2028		
	(0%)	(50%)	(100%)	(0%)	(50%)	(100%)
2.0	97.01	94.79	91.67	97.08	94.89	91.99
4.0	97.11	94.91	91.81	97.21	95.02	92.12
8.0	97.24	95.08	91.99	97.36	95.21	92.30
16.0	97.42	95.35	92.29	97.52	95.49	92.61
32.0	97.60	95.67	92.69	97.71	95.79	93.03
64.0	97.89	96.15	93.41	97.98	96.27	93.78
128.0	98.21	96.79	94.56	98.25	96.90	94.91
256.0	98.56	97.46	95.74	98.57	97.53	95.96
500.0	98.90	98.14	96.90	98.90	98.09	97.07
1000.0	99.38	98.72	97.93	99.48	98.70	97.89
1500.0	99.76	99.23	98.54	99.85	99.29	98.49
2000.0	99.95	99.65	99.06	99.98	99.74	99.10
2500.0	100.00	99.89	99.51	100.00	99.95	99.60
3000.0	100.00	99.99	99.81	100.00	100.00	99.88

The theoretical values are marked with “x” signs. The computed multiyear average solar illumination (for ephemeris data from 2009 to 2028) is marked with “+” signs. Lunar south pole sites are in blue and the lunar north pole sites are in red. The plotted values show reasonable agreement of computed values and theory, with the computed values usually less than the theoretical. Figure 38 shows the black curves of Equation (10) plotted parametrically with distance from the pole toward the nearside. The value of  $L_0$  was set to zero for the parametric curves. Figure 38 includes computed and theoretical values of the multiyear average DTE communications for the same sites as Figure 37, using the same symbol and color conventions.

No site has both 100 percent multiyear average solar illumination and 100 percent multiyear average DTE communications for a tower less than 1500 m tall. Towers of 1500 m at sites NB and NC will raise the multiyear average solar illumination to 100 percent. But for the lunar south pole sites, like B1, towers of over 2500 m are required to raise the multiyear average solar illumination to 100 percent. This is because the peaks Malapert  $\alpha$  and Leibnitz  $\beta$  obscure the view of the Sun from the lunar south pole. Equation (11) gives the elevation,  $H_p$ , above a spherical surface needed to see the winter Sun over a peak of elevation  $H_m$  at a distance,  $d$ , from the pole. Equation (11) provided values in Figures 4 and 37 for the Malapert  $\alpha$  and Leibnitz  $\beta$  peaks.

$$H_p = (R + H_m) \frac{\cos\left(\frac{180}{\pi} \frac{d}{R} - \alpha\right)}{\cos(\alpha)} - R \quad (11)$$

The obscuring effect of these peaks is also shown in Figure 5, where the peak Malapert  $\alpha$  appears at +10 deg azimuth.

**Table 6. Earth illumination metrics for site B1 tower heights.**

Tower height, m	Earth DTE Statistics, Assumed Uniform Distribution Multiyear Average Illumination			Earth DTE Statistics, Distribution from 2009 to 2028 Multiyear Average Illumination		
	(0%)	(50%)	(100%)	(0%)	(50%)	(100%)
2.0	65.16	58.24	51.33	63.47	58.61	53.95
4.0	65.16	58.25	51.33	63.48	58.61	53.96
8.0	65.17	58.26	51.35	63.49	58.62	53.97
16.0	65.20	58.29	51.37	63.51	58.63	53.98
32.0	65.25	58.34	51.42	63.54	58.67	54.01
64.0	65.35	58.44	51.52	63.61	58.74	54.08
128.0	65.56	58.64	51.73	63.75	58.88	54.21
256.0	65.96	59.05	52.13	64.04	59.14	54.47
500.0	66.74	59.82	52.91	64.60	59.66	54.97
1000.0	68.32	61.41	54.50	65.74	60.73	56.00
1500.0	69.91	63.00	56.08	66.91	61.81	57.03
2000.0	71.48	64.56	57.65	68.10	62.91	58.07
2500.0	73.04	66.12	59.21	69.33	64.01	59.12
3000.0	74.58	67.67	60.76	70.58	65.14	60.17

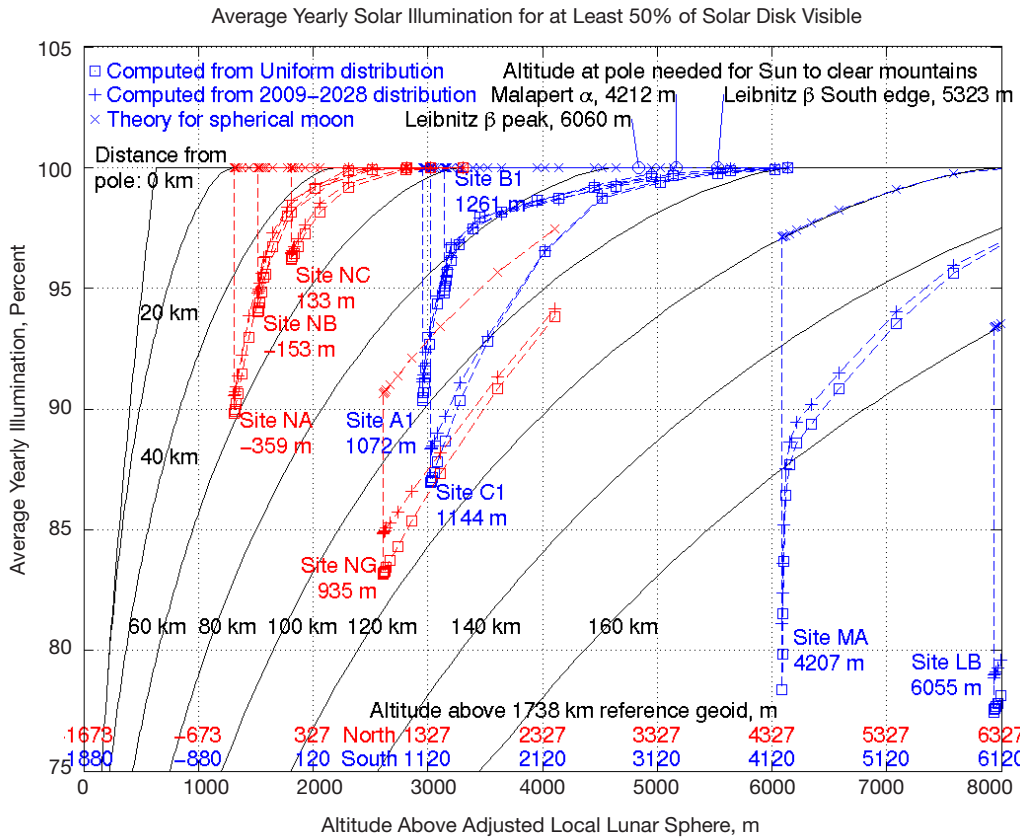


**Figure 37. Theory and computed values of multiyear average solar illumination.**

Figure 38 shows that the multiyear average DTE communication varies more with distance from the pole toward the prime meridian than with tower height above the local terrain. Towers up to 3000 m at the poles do not make significant improvements in the DTE communications average. At the lunar north pole, the computed multiyear average DTE communications for site NG exceeds the predicted values for towers between 32 and 1500 m tall. This is because the view toward the lunar nearside from site NG (at elevation 935 m) looks across the floor of Byrd Crater, which averages about -2500 m elevation.

The theory values generally correlate with the trends of the computed values, but are offset as much as 20 percent. This indicates that a theoretical model based on a spherical Moon does not capture the true physics of the horizon masks. The average elevation of a spherical model considers peaks and valleys in the terrain, but the peak elevations are the driving force behind the horizon mask visibility metrics. However, the convergence of the computed metrics with the theoretical metrics for the tallest towers is an expected result that lends confidence to the computed results.

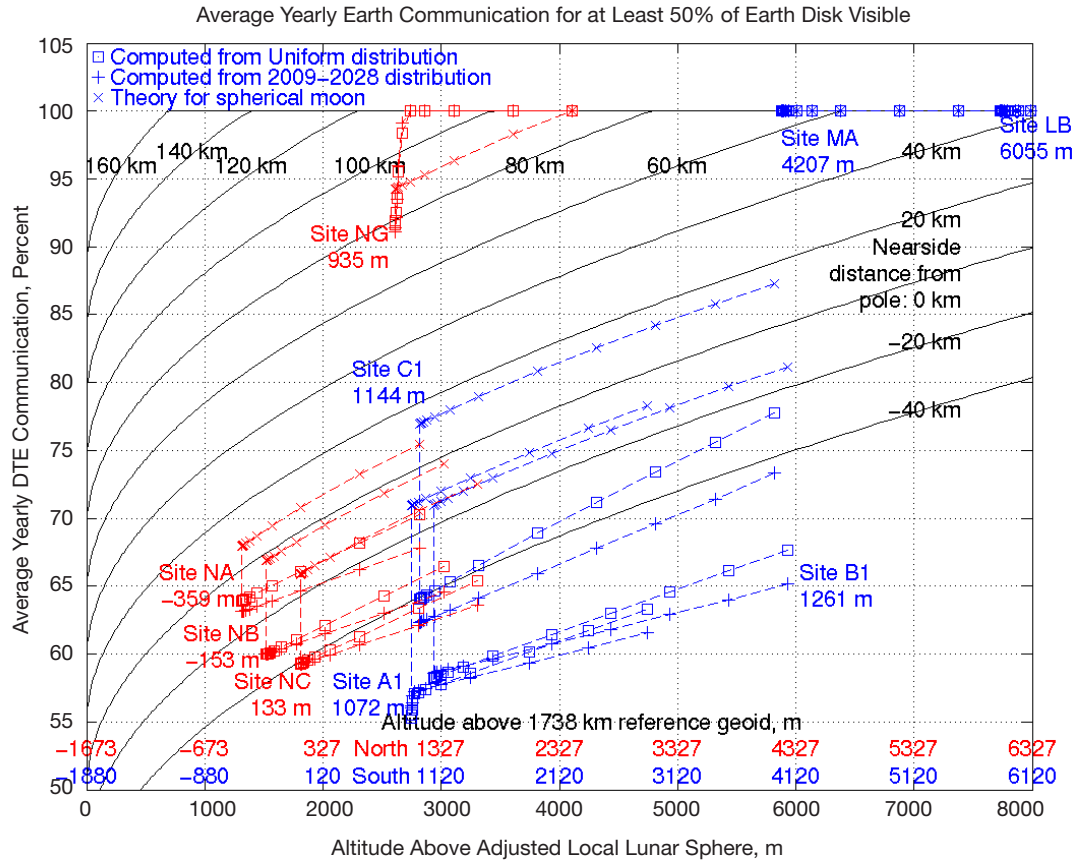


**Figure 38. Theory and computed values of multiyear average DTE communications.**

#### E. Considerations for Photovoltaic Array Design

The lunar pole sites create some difficult challenges for designing a continuously operating photovoltaic power system. The requirement to continually track the Sun could be met by installing the photovoltaic array on a vertical axle, oriented parallel to the lunar spin axis. At the lunar south pole, this axle would rotate counterclockwise with the Sun to keep the array normal to the solar radiation. This requires a foundation to support the axle, cross-beam structures to hold the array on the axle, and a drive system powerful enough to turn the array. This system also requires a solution to the “cable wrap” problem, in order to continually track the Sun. After 1 synodic month, the array has turned through 360 deg, and needs to continue rotating in the same direction. There are two basic approaches to this problem:

- (1) The “slip ring” solution: Power and control cables from the array go through multiple slip rings between the rotating array and the lunar surface. The design is complicated by the requirement to tolerate the fine dust on the lunar surface.
- (2) The “cable unwrap” solution: The array is rotated 360 deg clockwise to unwrap the cables. Using this method means stopping power production for a short amount of time, once per synodic month.

A heliostat design using a focusing mirror may provide a solution to the cable wrap problem [9]. This heliostat design may also produce a power system with lower mass than the other designs, because it does not need to support a rotating photovoltaic array. Figure 39 shows the heliostat design with the photovoltaic array installed horizontal to the local terrain. A parabolic mirror is installed above the array, angled at approximately 45 deg to the local horizontal. This mirror is suspended from the crossbar of a mast placed next to the array. The mast could also be the structure for the Lunar Communications Terminal (LCT) antennas. The mirror is suspended from an axle that is oriented parallel to the lunar spin axis. This axle rotates once per synodic month to continually reflect solar radiation onto the array. The mirror can continue to track the Sun after 360 deg revolution, since there are no cables attached to the moving part. This heliostat “periscope” design provides continuous solar tracking, but is partially shaded once per revolution when the Sun passes behind the support mast.

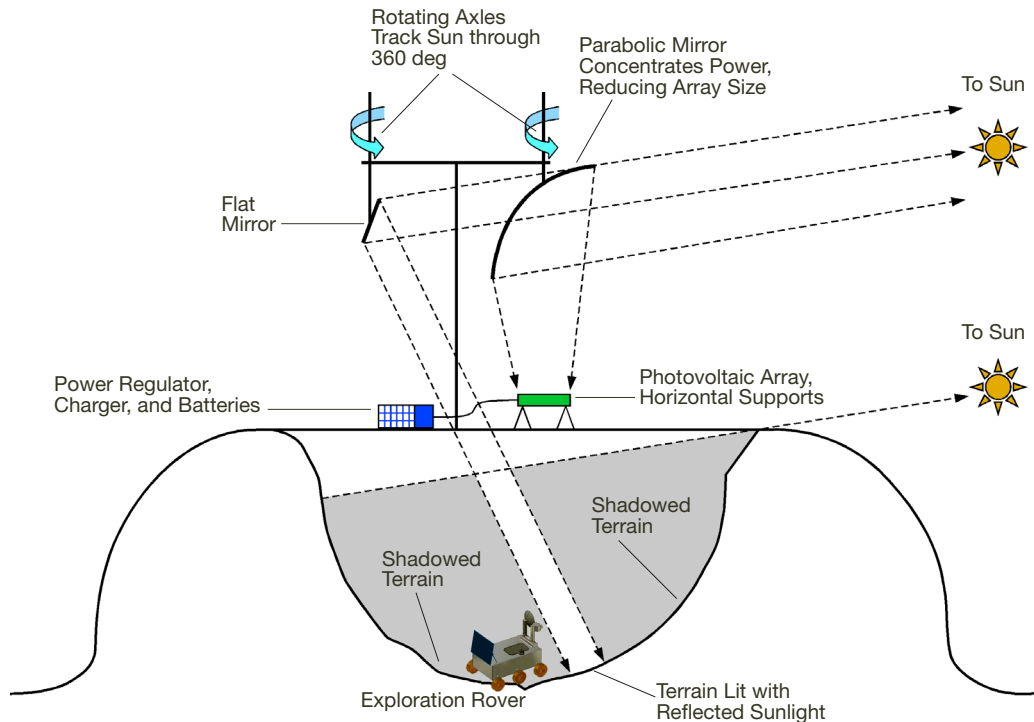


**Figure 39. Periscope mirror design to eliminate cable wrap.**

Shaping the mirror into a parabolic arc concentrates solar power for a small increase in mass. The trade-offs should consider the relative mass-per-unit area of the mirror and the photovoltaic panels, the reflectivity of the mirror material, and the relative masses of a rotating axle that supports the photovoltaic array versus supporting a mirror.

Additional flat periscope mirrors mounted on the crossbar could be used to direct solar light to areas nearby. This provides an efficient method of lighting work areas because it bypasses the inefficiencies of the photovoltaic system, battery storage, and electric lighting. If the photovoltaic power system is located on a crater rim (as in Figure 39), a flat periscope mirror could provide continuous lighting to exploration crews in the permanently shadowed areas within the crater. Sufficiently large heliostat mirrors could redirect enough sunlight to run photovoltaic arrays at remote locations. This would provide very efficient power transfer for operating within the permanently shaded areas. Transferring solar power with heliostat mirrors can also extend the mission operations time in the permanently shaded areas by removing the need to return to the base for recharging batteries.

#### **V. Conclusions**

Separating the lunar pole solar illumination problem into terrain horizon mask and solar motion computations simplified the production of illumination metrics. Using a simplified model of multiyear average solar motion allowed quick comparisons between potential human base locations at both lunar poles. The results show that within 100 km of the lunar south pole, solar illumination is maximized at previously identified site locations [3,4,5].

The best sites are on the rim of Shackleton Crater and the ridge west of Shackleton Crater. These three sites have multiyear average solar illumination between 90 and 97 percent. The sites have 100 percent solar power generation capability about 85 to 91 percent of the year. For both of these metrics, site B1 on the ridge west of Shackleton Crater has the highest multiyear average solar illumination values. Site B1 has DTE visibility of the entire Earth disk about 51 percent of each month. More detailed analysis of site B1 using the terrain horizon masks with more ephemeris data for the years 2009 to 2028 produced metrics that agreed with the uniform distribution approximations to within 5 percent. Specifically, the ephemeris data showed site B1 has a multiyear average of 100 percent solar power generation capability about 92 percent of the time. The ephemeris data computed a multiyear average DTE visibility of the entire Earth disk of about 54 percent of each month.

Examination of the site solar illumination profiles at 40-m resolution shows that the peaks of illumination are distributed over many points. The locations with greater than 80 percent solar illumination are spread over hundreds of meters. This supports the conclusion that the DEM has adequate sampling to show the true terrain characteristics.

#### **Acknowledgments**

The author expresses thanks to Martin A. Slade of JPL's GSSR group for his time and assistance with the 2006 GSSR DEM data. The author also wishes to thank Charles Ruggier and Laif Swanson of the System Concepts, Integration, and Planning (SCiP) Study Team at JPL for their support of this work.

## References

- [1] J. L. Margot, D. B. Campbell, R. F. Jurgens, and M. A. Slade, "Topography of the Lunar Poles from Radar Interferometry: A Survey of Cold Trap Locations," *Science*, vol. 284, pp. 1658–1660, June 4, 1999.
- [2] National Aeronautics and Space Administration, *The Vision for Space Exploration*, NP-2004-01-334-HQ, February 2004.  
[http://www.nasa.gov/pdf/55584main\\_vision\\_space\\_exploration-hi-res.pdf](http://www.nasa.gov/pdf/55584main_vision_space_exploration-hi-res.pdf)
- [3] M. Kruijff, "The Peaks of Eternal Light on the Lunar South Pole: How They Were Found and What They Look Like," 4th International Conference on Exploration and Utilization of the Moon (ICEUM4), ESA/ESTEC, SP-462, September 2000.
- [4] J. Fincannon, "Lunar South Pole Illumination: Review, Reassessment, and Power System Implications," 5th International Energy Conversion Engineering Conference and Exhibit (IECEC), AIAA 2007-4700, June 25–27, 2007.
- [5] J. Fincannon, "Characterization of Lunar Polar Illumination From a Power System Perspective," 56th AIAA Aerospace Sciences Meeting and Exhibit, AIAA 2008-0447, January 7–10, 2008.
- [6] M. Zuber and I. Garrick-Bethell, "What Do We Need to Know to Land on the Moon Again?" *Science*, vol. 310, pp. 983–985, November 11, 2005.
- [7] Scott Hensley, Eric Gurrola, Paul Rosen, Martin Slade, Joseph Jao, Micheal Kobrick, Raymond Jurgens, Eric De Jong, and Barbara Wilson, "Radar Generates High-Resolution Topographic Map of the Moon," *Society of Photo-Optical Instrumentation Engineers Newsroom*, June 16, 2008.
- [8] Ewan A. Whitaker, "The Lunar South Polar Regions," *Journal of the British Astronomical Association*, vol. 64, no. 6, pp. 234–242, 1954.
- [9] James D. Burke, "Merits of A Lunar Polar Base Location," *Lunar Bases and Space Activities of the 21st Century*, ed. W. W. Mendell, Lunar and Planetary Institute, Houston, Texas, 1985, p. 77.